

CTP and *parS* coordinate ParB partition complex dynamics and ParA-ATPase activation for ParABS-mediated DNA partitioning

James A Taylor^{1†}, Yeonee Seol², Jagat Budhathoki¹, Keir C Neuman², Kiyoshi Mizuuchi^{1*}

¹Laboratory of Molecular Biology, National Institute of Diabetes and Digestive and Kidney Diseases, National Institutes of Health, Bethesda, United States;

²Biochemistry and Biophysics Center, National Heart, Lung, and Blood Institute, National Institutes of Health, Bethesda, United States

Abstract ParABS partition systems, comprising the centromere-like DNA sequence *parS*, the *parS*-binding ParB-CTPase, and the nucleoid-binding ParA-ATPase, ensure faithful segregation of bacterial chromosomes and low-copy-number plasmids. F-plasmid partition complexes containing ParB_F and *parS*_F move by generating and following a local concentration gradient of nucleoid-bound ParA_F. However, the process through which ParB_F activates ParA_F-ATPase has not been defined. We studied CTP- and *parS*_F-modulated ParA_F-ParB_F complex assembly, in which DNA-bound ParA_F-ATP dimers are activated for ATP hydrolysis by interacting with two ParB_F N-terminal domains. CTP or *parS*_F enhances the ATPase rate without significantly accelerating ParA_F-ParB_F complex assembly. Together, *parS*_F and CTP accelerate ParA_F-ParB_F assembly without further significant increase in ATPase rate. Magnetic-tweezers experiments showed that CTP promotes multiple ParB_F loading onto *parS*_F-containing DNA, generating condensed partition complex-like assemblies. We propose that ParB_F in the partition complex adopts a conformation that enhances ParB_F-ParB_F and ParA_F-ParB_F interactions promoting efficient partitioning.

*For correspondence: kiyoshimi@nidk.nih.gov

Present address: †Alzheimer's Research UK Oxford Drug Discovery Institute, University of Oxford, Oxford, United States

Competing interests: The authors declare that no competing interests exist.

Funding: See page 25

Received: 10 December 2020

Preprinted: 25 January 2021

Accepted: 20 July 2021

Published: 21 July 2021

Reviewing editor: Thomas Surrey, Centre for Genomic Regulation (CRG), Spain

© This is an open-access article, free of all copyright, and may be freely reproduced, distributed, transmitted, modified, built upon, or otherwise used by anyone for any lawful purpose. The work is made available under the [Creative Commons CC0 public domain dedication](https://creativecommons.org/licenses/by/4.0/).

Introduction

Faithful segregation of replicated chromosomes is essential for efficient proliferation of cells. Accordingly, many bacteria are equipped with active chromosome and plasmid partition systems belonging to the ParABS family (Baxter and Funnell, 2014; Lutkenhaus, 2012; Vecchiarelli et al., 2012). Basic ParABS systems comprise two proteins, ParA and ParB, and a centromere-like, cis-acting DNA element called *parS*. The ParA proteins of this family are ATPases with a characteristic deviant Walker-A motif (Motallebi-Veshareh et al., 1990) and bind non-specific DNA (nsDNA) in an ATP-dependent manner by forming a DNA binding-competent dimer (Davey and Funnell, 1994; Leonard et al., 2005; Vecchiarelli et al., 2010). Accordingly, ParA proteins localize to the bacterial chromosome (the nucleoid) *in vivo* (Ebersbach and Gerdes, 2004; Hatano et al., 2007; Lim et al., 2014).

ParB is typically a dimeric sequence-specific DNA binding protein that binds tightly to the *parS* consensus sequences that mark the DNA cargo to be partitioned (Bouet et al., 2000; Mori et al., 1989; Pillet et al., 2011; Taylor et al., 2015). Most ParABS systems have multiple copies of a ParB dimer binding consensus sequence that collectively constitute a *parS* site. F-plasmid has a *parS* sequence cluster (*parS*_F, also called *sopC*) composed of 12 repeats of a 16 bp consensus sequence, each separated by 27 base-pair spacer sequences (Helsberg and Eichenlaub, 1986). The ParBs of

known chromosomal and plasmid Par systems such as P1 and F bind to *parS* via a helix-turn-helix motif (Schumacher and Funnell, 2005; Schumacher et al., 2010). These HTH-ParB proteins also associate with several kilobases of DNA surrounding a *parS* site *in vivo* in a proximity-dependent manner without obvious sequence specificity (Breier and Grossman, 2007; Murray et al., 2006; Rodionov et al., 1999; Sanchez et al., 2015). This activity, known as ParB spreading, is believed to be essential for proper function of these systems (Breier and Grossman, 2007; Graham et al., 2014) and results in the formation of a large nucleo-protein complex (the partition complex) around the *parS* site on the DNA to be partitioned. Mutations in the *B. subtilis parB* gene blocking spreading and causing partition deficiency have been identified within the Box II region (GXRR) of the N-terminal domain (Breier and Grossman, 2007; Graham et al., 2014), a highly conserved motif among HTH-ParB homologues (Yamaichi and Niki, 2000). Recently, several groups reported that HTH-ParB proteins have CTPase activity and the Box II residues play key roles in CTP binding and hydrolysis, suggesting that ParB spreading is driven by an active process dependent on energy derived from CTP hydrolysis (Jalal et al., 2020; Osorio-Valeriano et al., 2019; Soh et al., 2019).

ParB interacts with ParA via its N-terminal region (Ravin et al., 2003) and activates nsDNA-bound ParA dimer's ATPase, releasing it from DNA (Ah-Seng et al., 2009; Davis et al., 1992; Scholefield et al., 2011; Watanabe et al., 1992). In the absence of ParB stimulation, the ATP turnover of ParA is low, typically around one ATP per hour (Ah-Seng et al., 2009; Davis et al., 1992; Fung et al., 2001; Scholefield et al., 2011). Because of this slow basal ATPase rate, and since the majority of cellular ParB molecules is concentrated at the partition complexes due to ParB spreading, ATP hydrolysis by ParA and dissociation from the nucleoid is expected to occur principally in the vicinity of partition complexes. Biochemical studies of P1 ParA ATPase showed a significant time delay before activation of ParA for DNA binding after ATP binding, predicting a significant free bulk-diffusion period for ParA before reactivation for nsDNA binding (Vecchiarelli et al., 2010). This, along with *in vivo* imaging observations (Hatano et al., 2007; Ringgaard et al., 2009), led to a prediction that the nucleoid proximal to a partition complex would become depleted of ParA (the ParA depletion zone) and the proposal of a diffusion-ratchet model for plasmid segregation by the ParABS system (Vecchiarelli et al., 2010).

The diffusion-ratchet model is based on the premise that the nucleoid-bound ParA-ATPase activation by plasmid-bound ParB generates a local ParA depletion zone on the nucleoid, forming a nucleoid-bound ParA concentration gradient around the partition complex (Hu et al., 2017; Vecchiarelli et al., 2010). The interaction of plasmid-bound ParB with the ParA gradient on the nucleoid results in a cargo position-dependent free-energy difference (Sugawara and Kaneko, 2011). Binding of ParB to ParA reduces the system free-energy, therefore moving the cargo to a higher ParA concentration lowers the system free-energy. This cargo position-dependent free-energy difference translates to a directional motive force on the ParB bound cargo. The generation of sufficient cargo motive force to overcome thermal diffusion was demonstrated in cell-free reconstitution experiments showing that a bead coated with *parS_F*-containing DNA is driven across an nsDNA-coated flow cell surface in the presence of ParA_F, ParB_F, and ATP (Vecchiarelli et al., 2014). In some *in vivo* time-lapse imaging experiments, ParA has been observed to undergo pole-to-pole oscillations along the length of a nucleoid with a partition complex chasing the receding edge of a ParA distribution zone on the nucleoid, further supporting the diffusion-ratchet model (Hatano et al., 2007; Ringgaard et al., 2009). Variations of this model have also been proposed (Le Gall et al., 2016; Lim et al., 2014; McLeod et al., 2017).

Generating persistent directional motion by the diffusion-ratchet model requires a balance between the ParA-ParB association/dissociation dynamics prior to ATP hydrolysis and the steps and kinetic parameters that govern ATP hydrolysis. For example, if every ParA-ParB association resulted in instantaneous ATP hydrolysis and dissolution of the ParA-ParB bonds linking the partition complex (cargo) and the nucleoid, no cargo driving force would result. Conversely, if each bond persisted too long, the cargo would remain immobile on the nucleoid (Hu et al., 2017). However, the detailed biochemical reaction steps leading to ParB activation of DNA-bound ParA-ATPase and the subsequent release of ParA have not been determined.

In order to advance our quantitative understanding of the ParABS system mechanism, we investigated the assembly and disassembly kinetics of ParA_F-ParB_F complexes that form prior to ATP hydrolysis using F-plasmid ParA_FB_FS_F (also called SopA/B/C) as a model system. Employing a TIRF microscopy-based nsDNA-carpet assay (Vecchiarelli et al., 2013), we first examined the

stoichiometry of the nsDNA-bound ParA_F–ParB_F complexes that accumulate in the absence of ATP hydrolysis. We investigated impacts of different ParB_F-cofactors (*parS_F* and CTP) or ParB_F mutations that hinder ParB_F dimerization, *parS_F*-binding, CTPase activity, or ParA_F ATPase activation. We then studied how the same set of cofactors or ParB_F mutations influenced ParA_F-ATPase activation by ParB_F. Our results showed that ParB_F formed complexes with nsDNA-bound ParA_F in which both ParB_F-interacting faces of the ParA_F dimers were occupied by the N-terminal ParA_F-activation domain of ParB_F. All such complexes observed in the presence of ATPγS exhibited similar, slow dissociation kinetics from nsDNA compared to ParA_F dimers in the absence of ParB_F so long as both ParB_F-interacting faces of the ParA_F dimers were occupied by ParB_F N-terminal domains. Binding of ParB_F N-terminal domains at both ParB_F interaction faces is also necessary for efficient ATPase activation of nsDNA-bound ParA_F dimers. Strikingly, the ParB_F cofactors, CTP and *parS_F*, acted synergistically to accelerate the assembly of pre-ATP hydrolysis ParB_F–ParA_F complexes on nsDNA. In addition, a magnetic tweezers-based DNA condensation assay revealed that stable DNA condensation by ParB_F required both CTP and *parS_F*. These observations suggested that CTP and *parS_F* promote both ParA_F–ParB_F and ParB_F–ParB_F interactions. The compaction of *parS_F*-containing DNA by ParB_F in the presence of CTP recapitulated the salient features of the condensed ParB spreading partition complex observed *in vivo*, suggesting that ParB_F in the presence of *parS_F* and CTP closely reflects the functional state of ParB_F in the partition complexes *in vivo*. Interestingly, ParB_F in these conditions accelerated ATP turnover by the nsDNA-bound ParA_F no more than twofold compared to ParB_F without *parS_F* and CTP, to a modest ~80 h⁻¹. These findings have important implications for the diffusion-ratchet model of F-plasmid partition by the ParABS system.

Results

Here, we investigated the ParA–ParB interactions that lead to accelerated ATP hydrolysis by ParA and how they are impacted by *parS_F* and CTP. First, we addressed the nature of nsDNA-bound ParA_F–ParB_F complexes. In the presence of ATP, ParA_F forms DNA binding-competent dimers and binds the nsDNA-carpet without ParB_F. Upon forming a complex with ParB_F, ParA_F becomes activated for ATP hydrolysis and the complex rapidly disassembles (Vecchiarelli *et al.*, 2013), impeding characterization of the complex. Therefore, we studied DNA-bound ParA_F–ParB_F complexes that accumulate prior to ATP hydrolysis by using non-hydrolysable ATPγS. ParA_F is not expected to form DNA binding competent dimers efficiently in the presence of ATPγS based on the study of the closely related ParA_{P1} ATPase (Vecchiarelli *et al.*, 2010). However, we found ParB_F promotes conversion of ParA_F to a DNA binding competent state in the presence of ATPγS (see below). Hence, in this study, we infused ParA_F-eGFP and ParB_F-Alexa647, or other fluorescent-labeled ParB_F variants, preincubated at room temperature for 10 min with ATPγS into an nsDNA-carpeted flow cell and quantified the densities of the two DNA-associated proteins by imaging the flow cell surface with TIRF microscopy (Figure 1). ParA_F alone at the concentration used here (1 μM, all protein concentrations are expressed as monomer concentrations) does not efficiently bind DNA in the presence of ATPγS as expected, and only low-level steady state density (less than ~200 monomers per μm²) of ParA_F-eGFP was detected on the DNA-carpet (Figure 2A,B). The observed DNA dissociation rate constant of ParA_F-ATPγS (~6 min⁻¹) is similar to that of ParA_F-ATP estimated by FRAP or by washing the flow-cell with nsDNA-containing buffer (~4.5–6 min⁻¹, Vecchiarelli *et al.*, 2013). ParB_F-Alexa647 (2 μM) did not bind the DNA-carpet to a significant level in the 300 mM K-glutamate buffer used in this experiment.

The N-terminus of ParB_F alone enhances DNA binding activity of ParA_F

We first examined if the N-terminal ParA_F-activation domain of ParB_F (ParB_F¹⁻⁴²) alone can induce the ParA_F conformational changes necessary for DNA binding in the presence of ATPγS. The activation domain includes Arginine 36, which is critical for activation of ParA_F ATPase (Ah-Seng *et al.*, 2009; Leonard *et al.*, 2005), but lacks the CTPase (AA63-155), *parS_F*-binding (AA160-272), and dimerization (AA276-323) domains. For these experiments, we used ParB_F¹⁻⁴² fused to the N-terminus of mCherry (ParB_F¹⁻⁴²-mCherry). This protein is a monomer in solution as judged by its elution profile on a gel filtration column (Figure 2—figure supplement 1). ParB_F¹⁻⁴²-mCherry (10 μM) and ParA_F-eGFP (1 μM) bound the DNA-carpet together in the presence of ATPγS to a density of ~5000 monomers/μm² maintaining ~1:1 stoichiometry (Figure 2C). When washed with a buffer containing ATPγS, ParB_F¹⁻

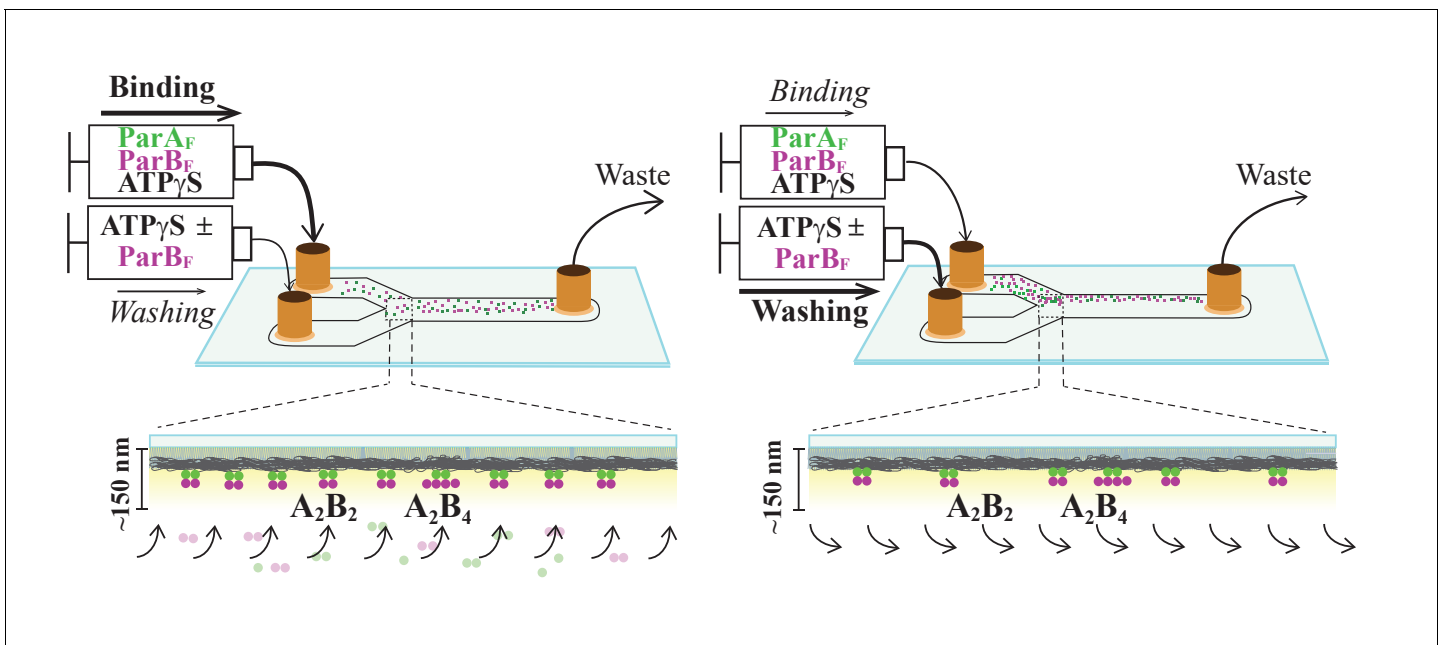


Figure 1. Schematic of flow cell setup for visualizing the binding and dissociation of fluorescent proteins on DNA-carpet. ParA_F-eGFP and ParB_F-Alexa647 proteins were flowed over a dense carpet of nsDNA attached to the supported lipid bilayer coated surface of a flow cell. TIRF microscopy permits selective detection of the DNA-carpet bound proteins. Sample solution and wash buffer, as specified for each experiment, were infused via two syringes at different infusion rates from separate inlets into a Y-shaped flow cell. A laminar boundary separates the two solutions downstream of the flow convergence point at the Y-junction. At the midpoint across the flow channel, downstream but close to the flow convergence point where the observations are made, the DNA-carpet area is exposed to the syringe content of the higher infusion rate. When the infusion rates of the two syringes are switched, the laminar boundary moves across the observation area and the solution flowing over the area switches. By switching the infusion rates of the two syringes repeatedly, multiple DNA-carpet-bound protein complex assembly and wash cycles can be recorded.

⁴²-mCherry dissociated first, with an apparent dissociation rate constant of $\sim 5.7 \text{ min}^{-1}$, closely followed (within a few seconds) by ParA_F-eGFP dissociation (Figure 2D). On the other hand, when the wash buffer contained $10 \mu\text{M}$ ParB_F¹⁻⁴²-mCherry and ATP γ S, both proteins dissociated together, significantly slower than ParA_F-eGFP bound to the DNA-carpet alone, with an apparent rate constant of $\sim 0.9 \text{ min}^{-1}$, maintaining $\sim 1:1$ stoichiometry (Figure 2E). After essentially complete dissociation of ParA_F-eGFP from the DNA-carpet, $10 \mu\text{M}$ ParB_F¹⁻⁴²-mCherry present in the wash solution showed no significant binding to the DNA-carpet, indicating low intrinsic affinity of this protein for DNA. FRAP measurements of ParA_F-eGFP—ParB_F¹⁻⁴²-mCherry bound in steady state to the DNA-carpet in the presence of ATP γ S also indicated rapid exchange of ParB_F¹⁻⁴²-mCherry (Figure 2—figure supplement 2). Thus, at saturating ParB_F¹⁻⁴²-mCherry concentration, a ParA_F—ATP γ S dimer is bound by two molecules of ParB_F¹⁻⁴²-mCherry occupying both sides of the ParA_F dimer. The data also indicate that ParA_F dimers adopt a state of slowed dissociation from nsDNA when both of the ParB_F-interacting faces are occupied by the ParB_F N-terminal domain. The nsDNA dissociation rate constants of ParA_F—ParB_F complexes (including those involving ParB_F variants) and ParB_F:ParA_F stoichiometry reported above and in the following sections are summarized in Table 1.

ParA_F ATPase activation requires binding of two copies of ParB_F N-terminal domain to the ParA_F dimer

ParB_F¹⁻⁴² stimulated ParA_F-ATPase ($1 \mu\text{M}$) with a clear sigmoidal ParB_F¹⁻⁴² concentration dependence and a half-maximum activation concentration of $\sim 1.2 \mu\text{M}$ (Figure 2F; Table 2). Thus, monomeric ParB_F¹⁻⁴² appears to activate ParA_F-ATPase when it binds on both sides of the DNA-bound ParA_F dimers. To test whether the observed sigmoidal concentration dependence is due to the monomeric nature of ParB_F¹⁻⁴², we prepared the N-terminal region of ParB_F fused to mCherry and the nuclease activity deficient EcoRI^{E111Q}, ParB_F¹⁻⁴²-mCherry-EcoRI^{E111Q} (see Figure 2—figure supplement 3A). This construct, with expected EcoRI dimerization $K_D < 20 \text{ pM}$ (Modrich and Zabel, 1976), efficiently

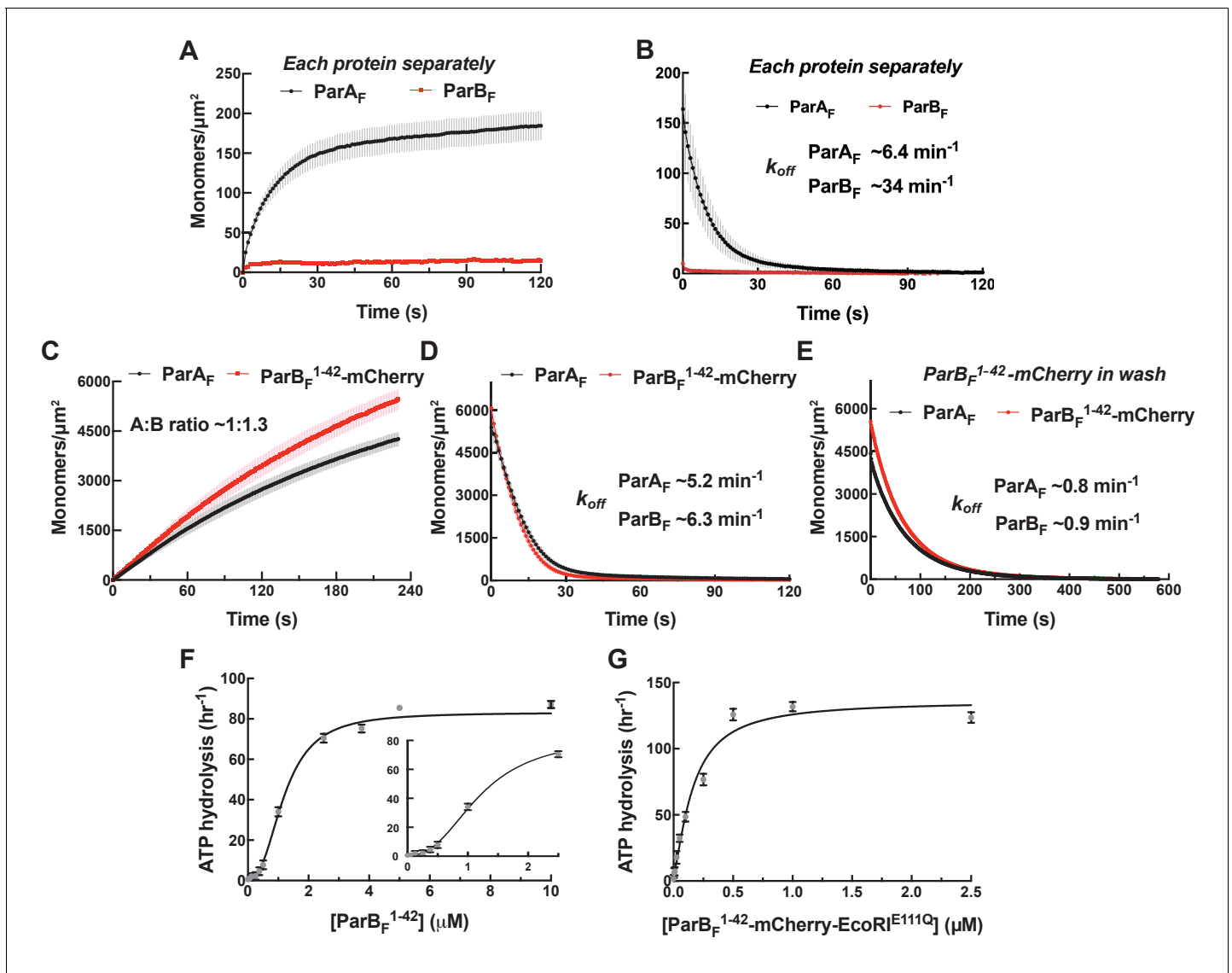


Figure 2. Monomeric ParB_F¹⁻⁴²-mCherry can activate ParA_F for nsDNA binding in the presence of ATPγS by forming a ~1:1 complex. Protein sample solution in the presence of ATPγS (1 mM) was infused into nsDNA-carpeted flow cell at a constant flow to monitor the protein binding to the nsDNA, and the sample solution was switched to a wash buffer containing ATPγS to monitor protein dissociation from nsDNA. (A, B) Binding to, and dissociation from, nsDNA of ParA_F-eGFP (1 μM) or ParB_F-Alexa647 (2 μM) were measured separately. (C) ParB_F¹⁻⁴²-mCherry (10 μM) and ParA_F-eGFP (1 μM) preincubated with ATPγS were infused into the nsDNA-carpeted flow cell and (D) washed with buffer containing ATPγS. (E) The washing experiment of (D) was repeated with wash buffer containing ATPγS and ParB_F¹⁻⁴²-mCherry (10 μM). For the parameters of the time courses of above experiments and subsequent experiments of the same type in this study, see **Table 1**. The ParB_F:ParA_F ratio was calculated from carpet-bound densities of the two proteins measured in parallel, and summarized in **Table 1**. (F) ParA_F-ATPase activity (expressed as turnover rate per ParA_F monomer) was measured in the presence of EcoRI-digested pBR322 DNA (60 $\mu\text{g}/\text{ml}$) and different concentrations of ParB_F¹⁻⁴². Inset shows a plot with expanded abscissa. (G) ParA_F-ATPase activity was measured as above in the presence of dimeric ParB_F¹⁻⁴²-mCherry-EcoRI^{E111Q}. The parameters of ATPase stimulation curves in these and subsequent figures are summarized in **Table 2**.

The online version of this article includes the following figure supplement(s) for figure 2:

Figure supplement 1. Gel filtration column elution profile of ParB_F¹⁻⁴²-mCherry.

Figure supplement 2. FRAP of ParA_F-eGFP and ParB_F¹⁻⁴²-mCherry on DNA-carpet.

Figure supplement 3. Comparison of possible structural domain arrangements of artificially dimeric ParB_F¹⁻⁴²-mCherry-EcoRI^{E111Q}.

Figure supplement 4. ParA_F ATPase stimulation by ParB_F¹⁻⁴²-mCherry-EcoRI^{E111Q} is not influenced by the addition of DNA fragment containing EcoRI recognition sequence.

Table 1. Apparent disassembly or exchange rate constants (min^{-1}) and $\text{ParB}_F/\text{ParA}_F$ ratio from fits of TIRFM wash and FRAP experiments. The apparent dissociation (or FRAP) rate constants (k_{off}) were obtained for individual time-trajectories by single-exponential curve fitting (except ** where the rate of the faster decay, $(68 \pm 0.5\%)$ of a double-exponential fit is shown), and the mean and SEM for the set of independent experiments are shown (except * where standard deviation among non-independent repeats within an experiment is shown). (N is the number of separate experiments, with total number of binding/wash cycles for repeated data collection in parenthesis.) $\text{ParA}:\text{ParB}$ ratios were calculated from the final phase of the individual association time-trajectories (except *** where it was based on the beginning part of the washing phase in the presence of ParB_F^{1-42} R36A), and the mean and SEM for the set of independent experiments are shown in italics. N.D., not done.

Protein Measured	ParA_F		$\text{ParA}_F + \text{ParB}_F^{1-42}$		$\text{ParA}_F + \text{ParB}_F^{1-42}$ R36A		FRAP		$\text{ParA}_F + \text{ParB}_F$		$\text{ParA}_F + \text{ParB}_F + \text{CDP}$		$\text{ParA}_F + \text{ParB}_F + \text{CTP}$		$\text{ParA}_F + \text{ParB}_F^{121A}$			
	k_{off}	ParA_F	k_{off}	ParA_F	k_{off}	ParA_F	ParB_F^{1-42}	ParA_F	ParB_F	k_{off}	ParA_F	k_{off}	ParA_F	ParB_F	k_{off}	ParA_F	ParB_F^{121A}	
- parS_F																		
k_{off}	6.4 ± 0.6 N=4 (12)	5.2 ± 0.2 N=2 (9)	6.3 ± 0.3 N=2 (9)	29 ± 2 N=3 (9)	2.0 ± 0.08 N=3 (11)	2.0 ± 0.08 N=3 (11)	$15.3 \pm 2.1^{**}$ N=3 (12)	0.93 ± 0.07 N=2 (6)	0.89 ± 0.09 N=2 (6)	N.D.	N.D.	N.D.	0.63 ± 0.04 N=2 (7)	0.65 ± 0.10 N=2 (7)	0.89 ± 0.01 N=3 (8)	0.89 ± 0.01 N=3 (8)	0.78 ± 0.05 N=3 (8)	
A:B	$1 : 1.27 \pm 0.06$ N=2 (8)		$1 : 0.92 \pm 0.02^{***}$ N=3 (9)		$1 : 0.92 \pm 0.02^{***}$ N=3 (9)		$1 : 1.10 \pm 0.13$ N=3 (9)		$1 : 2.16 \pm 0.15$ N=3 (10)		$1 : 2.16 \pm 0.15$ N=3 (10)		$1 : 0.99 \pm 0.01$ N=3 (8)		$1 : 0.99 \pm 0.01$ N=3 (8)		$1 : 0.99 \pm 0.01$ N=3 (8)	
k_{off}	N.D.	N.D.	N.D.	N.D.	N.D.	N.D.	0.95 ± 0.04 N=2 (6)	0.82 ± 0.01 N=2 (6)	0.46 ± 0.02 N=2 (7)	0.53 ± 0.01 N=2 (7)	0.60 ± 0.08 N=2 (5)	0.83 ± 0.12 N=2 (6)	0.91 ± 0.01 N=3 (8)	0.78 ± 0.04 N=3 (8)	0.78 ± 0.04 N=3 (8)	0.78 ± 0.04 N=3 (8)	0.78 ± 0.04 N=3 (8)	0.78 ± 0.04 N=3 (8)
A:B	$1 : 2.17 \pm 0.40$ N=3 (9)		$1 : 2.53 \pm 0.07$ N=2 (6)		$1 : 2.53 \pm 0.07$ N=2 (6)		$1 : 2.16 \pm 0.27$ N=2 (6)		$1 : 1.12 \pm 0.01$ N=3 (12)		$1 : 1.12 \pm 0.01$ N=3 (12)		$1 : 1.12 \pm 0.01$ N=3 (12)		$1 : 1.12 \pm 0.01$ N=3 (12)		$1 : 1.12 \pm 0.01$ N=3 (12)	
ParB_F or ParB_F^{1-42} R36A in wash	$0.84 \pm 0.01^*$ N=1 (3)	$0.89 \pm 0.02^*$ N=1 (3)	1.8 ± 0.4 N=3 (9)	1.8 ± 0.4 N=3 (9)	N.D.	N.D.	N.D.	N.D.	N.D.	N.D.	N.D.	N.D.	N.D.	N.D.	N.D.	N.D.	N.D.	N.D.

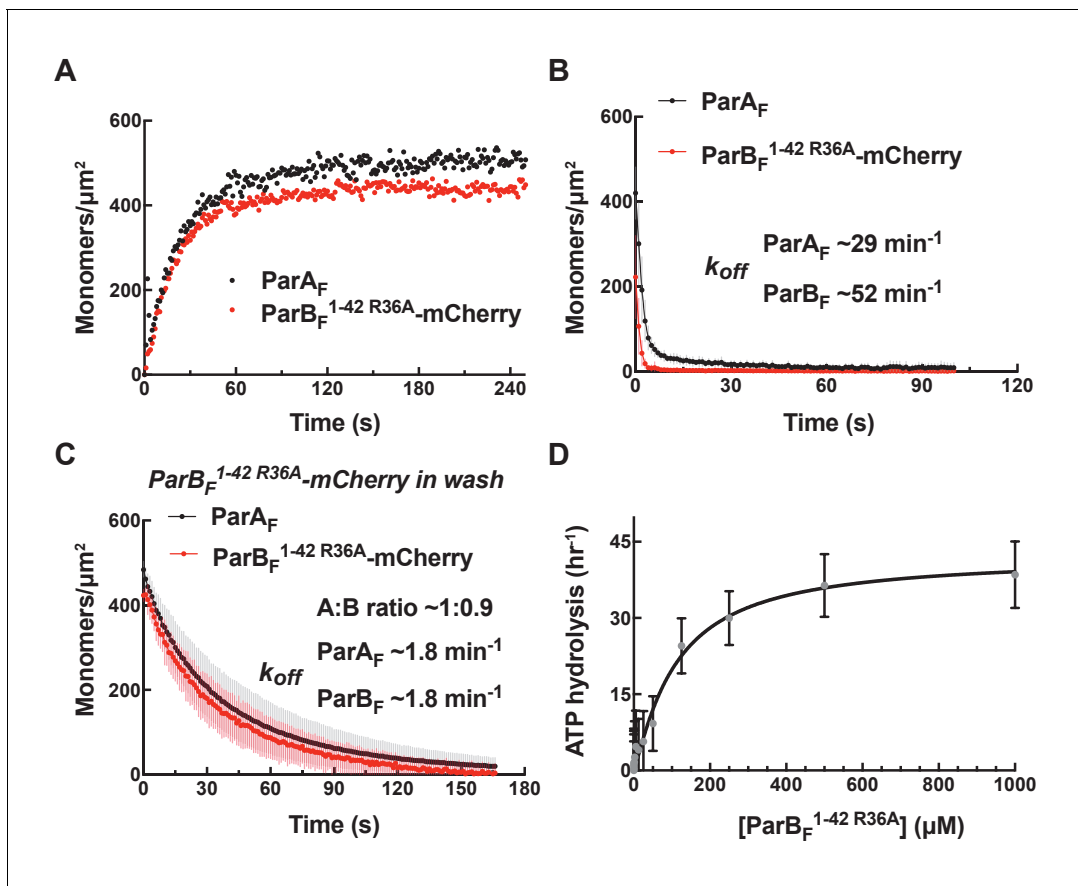


Figure 3. ParB_F^{1-42 R36A}-mCherry dissociates faster from nsDNA-carpet-bound ParA_F-ATPγS dimer, and ParA_F-ATPase activation requires higher ParB_F^{1-42 R36A} concentration. (A) ParB_F^{1-42 R36A}-mCherry (10 μM) and ParA_F-eGFP (1 μM) preincubated with ATPγS were infused into the nsDNA-carpeted flow cell and then (B) washed with buffer containing ATPγS. (C) The washing experiment of B was repeated with buffer containing ATPγS and ParB_F^{1-42 R36A}-mCherry (10 μM). (D) ParA_F-ATPase activity was measured in the presence of EcoRI-digested pBR322 DNA (60 μg/ml) as a function of ParB_F^{1-42 R36A} concentration. See **Figure 2** legend and **Tables 1** and **2** for additional details.

activated ParA_F-ATPase at least to a similar maximum rate as ParB_F¹⁻⁴², but with a *K*_{half} of ~0.15 μM, ~eight fold lower than ParB_F¹⁻⁴², and displayed no noticeable sigmoidal concentration dependence (**Figure 2G**). Potential binding of the inactive EcoRI domain to DNA did not appear to influence the ATPase activation properties of this construct; addition of EcoRI-binding DNA fragment in the reaction did not impact the ATPase activation (**Figure 2—figure supplement 4**). Based on these results, we conclude that both ParB_F-binding faces of a ParA_F dimer must be occupied by ParB_F N-termini for stimulation of its ATPase activity.

ParB_F^{1-42 R36A} forms a rapidly disassembling complex with ParA_F on the DNA carpet

An R36A mutation was reported to significantly compromise ParB_F's ability to activate ParA_F's ATPase (**Ah-Seng et al., 2009**). To test whether this mutation affected ParB_F's ability to form a complex with ParA_F we repeated the experiments shown in **Figure 2C–E** using ParB_F^{1-42 R36A}-mCherry. ParB_F^{1-42 R36A}-mCherry and ParA_F-eGFP bound with an approximately 1:1 stoichiometry, similar to ParB_F¹⁻⁴²-mCherry but reached a steady-state density on the DNA-carpet of less than 10% of the density observed with ParB_F¹⁻⁴²-mCherry (**Figure 3A**). When washed with buffer containing ATPγS, ParB_F^{1-42 R36A}-mCherry dissociated first followed by ParA_F, similar to the results obtained with ParB_F¹⁻⁴²-mCherry but ParB_F^{1-42 R36A}-mCherry dissociated ~10-fold faster, followed by dissociation of ParA_F-eGFP within a few seconds (**Figure 3B**). When the wash buffer also contained 10 μM ParB_F^{1-42 R36A}-mCherry the two proteins dissociated in parallel maintaining ~1:1 stoichiometry (**Figure 3C**). Together these observations indicate that ParB_F^{R36A}

Table 2. ATPase fit parameters.

ATPase measurements were performed with ParA_F (1 μM) and different mutants of ParB_F, 60 μg/ml EcoRI-digested pBR322 DNA plus Scram- or *parS*_F-DNA fragment and CTP or CDP, as indicated in the column headings. Assays were repeated 'N' times, each data set of an assay was fit after subtraction of background measured without ParA_F to a modified Hill equation: $v - v_0 = (v_{max} [B]^n) / (K_A^n + [B]^n)$, and the mean and standard error of the mean (SEM) of the fit parameters for the N measurements are shown. For [B] on the x-axis, total ParB_F concentration was used instead of free ParB_F concentration due to technical issues in estimating the free ParB_F concentration and the meanings of K_A and the cooperativity factor (n) here differ from those in the standard adaptation of the Hill equation. v_{max} is the maximum stimulated ParA_F ATPase turnover rate, K_A is the apparent total concentration of ParB_F necessary for half maximum stimulation, and n is the apparent cooperativity coefficient.

DNA cofactor Number of exp.	ParB _F		ParB _F CTP		ParB _F CDP	ParB _F ^{R121A}		ParB _F ¹⁻⁴² 42	ParB _F ¹⁻⁴² R36A	ParB _F ¹⁻⁴² -mCherry- EcoRI ^{E111Q}	EcoRI DNA
	Scram N = 6	<i>parS</i> _F N = 6	Scram N = 3	<i>parS</i> _F N = 3	<i>parS</i> _F N = 3	Scram N = 3	<i>parS</i> _F N = 3	N = 6	N = 3	Scram N = 3	N = 2
v_{max} (hr ⁻¹)	54 ± 5	79 ± 2	79 ± 8	78 ± 8	87 ± 5	60 ± 5	62 ± 5	83 ± 3	38 ± 2	131 ± 13	125 ± 9
K _A (μM)	0.53 ± 0.09	0.59 ± 0.03	0.41 ± 0.05	0.24 ± 0.02	0.34 ± 0.04	0.86 ± 0.1	1.1 ± 0.1	1.2 ± 0.1	108 ± 13	0.16 ± 0.04	0.16 ± 0.03
Cooperativity coefficient (n)	1.2 ± 0.2	1.4 ± 0.1	3.3 ± 1.0	3.6 ± 0.2	1.1 ± 0.1	2.5 ± 0.6	1.6 ± 0.3	2.5 ± 0.3	1.5 ± 0.2	1.4 ± 0.3	1.4 ± 0.2

interacts with ParA_F, but with a much faster dissociation rate constant compared to wild-type ParB_F. ParB_F^{1-42 R36A} could activate ParA_F-ATPase with an increased half-saturation concentration of 108 μM, approximately 100-fold higher than ParB_F¹⁻⁴² (Figure 3D). These results explain the puzzling report that while the R36A mutation severely compromised activation of ParA_F-ATPase by ParB_F, it did not impede oscillation of ParA_F on the nucleoid, and only mildly reduced plasmid stability (Ah-Seng et al., 2013). At the interface between the ParA_F-bound nucleoid and partition complexes containing many ParB_F dimers, the local ParB_F concentration is expected to be sufficiently high for this mutant protein to activate ParA_F-ATPase to effectively generate a ParA_F depletion zone and motive force driving the partition complex as indicated by the repeated oscillation of the nucleoid-bound ParA_F distribution.

ParA_F and ParB_F bind to and dissociate from nsDNA together in the presence of ATPγS with ~ 1:1 stoichiometry

When ParA_F-eGFP and full-length ParB_F-Alexa647 were incubated together at 1 μM and 2 μM, respectively, in the presence of ATPγS, they bound to the DNA-carpet in parallel maintaining ~1:1 stoichiometry up to a density of ~5000 monomers/μm² (Figure 4A). They also dissociated from the DNA-carpet in parallel, maintaining ~1:1 stoichiometry, when washed with a buffer containing ATPγS, with an apparent dissociation rate constant of approximately ~1 min⁻¹ (Figure 4B). These results show that ParA_F and ParB_F form a hetero-tetramer containing two monomers each of ParA_F and ParB_F (A₂B₂), or larger oligomers composed of the hetero-tetramers, that binds as a unit on nsDNA in the presence of ATPγS.

Full-length ParB_F, which forms dimer with apparent K_D of ~ 19 nM (Figure 4—figure supplement 1), activated ParA_F-ATPase in the presence of nsDNA to ~50 hr⁻¹ without significant sigmoidal concentration dependence (Figure 4E). Based on the results of experiments with monomeric ParB_F¹⁻⁴² proteins described earlier, we conclude that a single dimer of full-length ParB_F can straddle an nsDNA-bound ParA_F dimer, permitting the two N-termini to interact with both of the ParB_F-binding faces of the ParA_F dimer to activate the ATPase.

In the presence of *parS*_F, ParB_F forms a 2:1 complex with ParA_F

We next asked if ParB_F bound to *parS*_F interacts differently with ParA_F on the DNA-carpet. We preincubated ParA_F-eGFP, ParB_F-Alexa647, ATPγS and a 24 bp duplex DNA fragment containing a single *parS*_F consensus sequence, at a slight molar excess over ParB_F dimer, for 10 min at room temperature. At the concentrations used, most of the ParB_F dimers are expected to be bound to *parS*_F. When infused into the DNA-carpeted flow cell, ParA_F-eGFP and ParB_F-Alexa647 bound to and

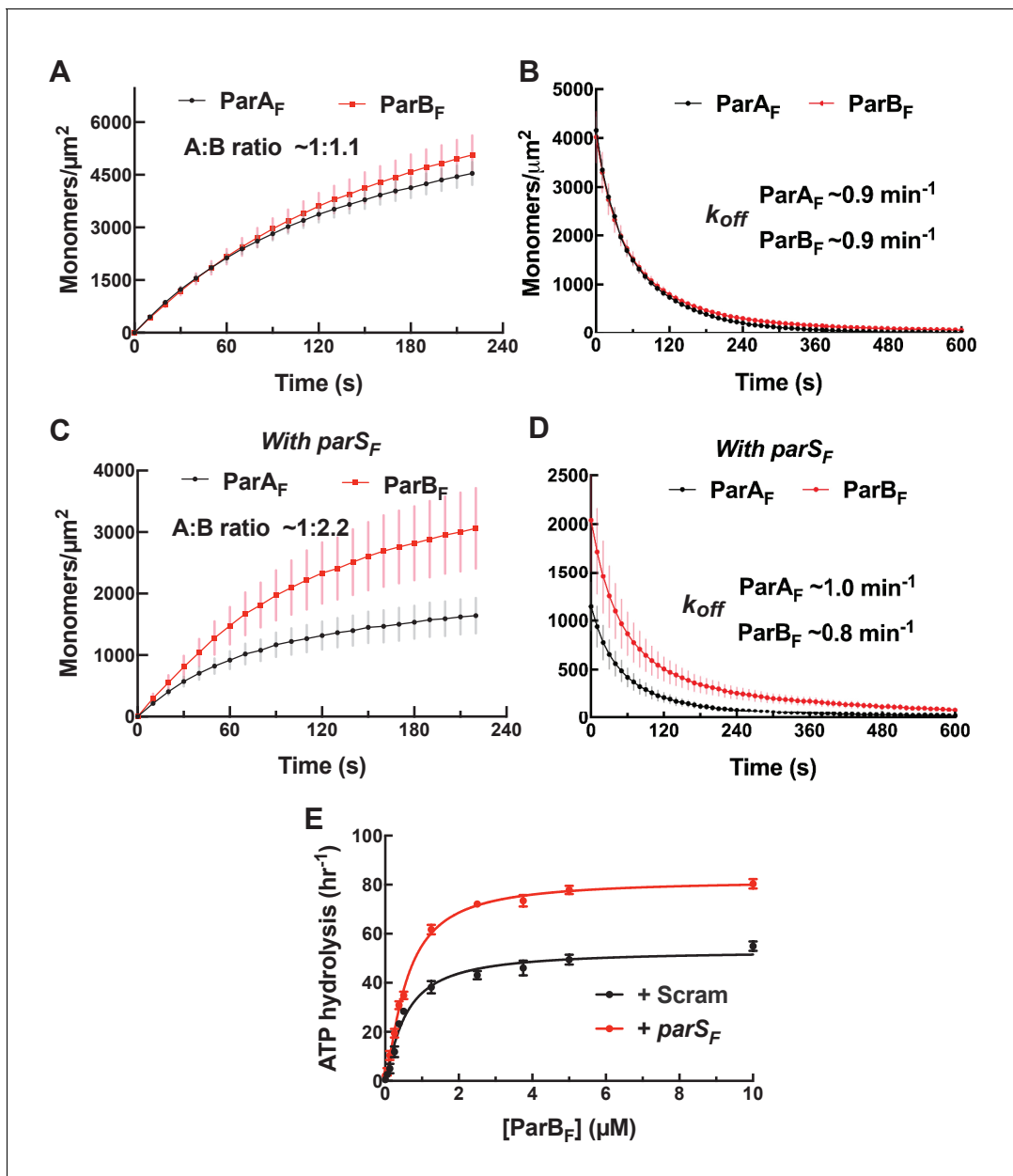


Figure 4. *parS_F* DNA alters protein stoichiometry of the ParA_F-ParB_F complex formed prior to ATP hydrolysis and the extent of ParA_F-ATPase activation by ParB_F. (A) ParA_F-eGFP (1 μM) and ParB_F-Alexa647 (2 μM) preincubated with ATP γ S were infused into the nsDNA-carpeted flow cell and then (B) washed with buffer containing ATP γ S. (C, D) As (A) and (B) except the sample included the 24 bp *parS_F* DNA fragment (1.1 μM). (E) ParA_F-ATPase activity was measured in the presence of EcoRI-digested pBR322 DNA (60 $\mu\text{g}/\text{ml}$), different concentrations of ParB_F and either a *parS_F*-DNA fragment or a DNA fragment with a scrambled sequence (1.1-fold higher concentrations than the ParB_F dimers). See **Figure 2** legend and **Tables 1** and **2** for additional details.

The online version of this article includes the following figure supplement(s) for figure 4:

Figure supplement 1. Determination of ParB_F monomer-dimer K_D by FRET.

Figure supplement 2. Mutation of a BoxII residue R121A does not affect the affinity of ParB_F^{R121A} for *parS_F*, but neither the protein stoichiometry of the ParA_F-ParB_F^{R121A} complex assembled on nsDNA prior to ATP hydrolysis, nor the extent of ParA_F-ATPase activation by ParB_F^{R121A} is impacted by the presence of *parS_F*.

dissociated from the carpet with a stoichiometry of $\sim 1:2$ (**Figure 4C,D**), in sharp contrast to the $\sim 1:1$ stoichiometry without *parS_F* DNA. The kinetic parameters of the complex assembly and disassembly were not significantly affected. These results demonstrate that ParA_F and ParB_F form a complex of one ParA_F dimer and two ParB_F dimers (A₂B₄) in the presence of *parS_F*.

Does the change in protein stoichiometry caused by *parS_F* translate to different levels of ParA_F-ATPase activation? A previous study, comparing plasmid DNA with and without *parS_F* as the cofactor, showed that ParB_F activates ParA_F-ATPase a few-fold more efficiently in the presence of plasmid DNA containing a full *parS_F* site (**Ah-Seng et al., 2009**). We titrated ParB_F in the presence of ParA_F, pBR322 DNA, and 24 bp *parS_F* duplex at a stoichiometric excess concentration over the ParB_F dimer. In the presence of *parS_F* DNA, ParB_F activated ParA_F-ATPase to a maximum turnover rate of $\sim 80 \text{ hr}^{-1}$, a $\sim 60\%$ increase compared to reactions where the *parS_F* fragment was replaced with a scrambled sequence fragment (**Figure 4E**). These results indicate that a single *parS_F* DNA-bound ParB_F dimer cannot straddle an nsDNA-bound ParA_F dimer to activate the ATPase, but by binding two ParB_F dimers the ATPase activation level reaches slightly higher level than in the absence of *parS_F* DNA.

We note that ParB_F^{R121A}, harboring a mutation in the conserved Box II region of the CTPase domain, neither exhibited a change in the ParB_F/ParA_F complex stoichiometry, nor a change in the ParB_F-stimulated ATP turnover, in response to *parS_F* (**Figure 4—figure supplement 2**), suggesting that the effects of *parS_F* binding described above are mediated through conformational changes in the CTPase domain (see below for further discussion).

CTP alters the complex formed between ParA_F and ParB_F in a manner similar to *parS_F* and accelerates complex formation in the presence of *parS_F*

ParB proteins have recently been reported to have CTPase activity that is coupled with changes in their DNA binding properties and refolding of the CTPase domains into a globular dimeric structure in the presence of CTP (**Soh et al., 2019; Osorio-Valeriano et al., 2019**) from the more extended and poly-dispersed structure in the absence of nucleotide (**Chen et al., 2015**). We therefore decided to test whether the addition of CTP influences the ParA_F-ParB_F complex formed on the DNA-carpet in the presence of ATP γ S. When ParA_F-eGFP and ParB_F-Alexa647 were incubated together in the presence of ATP γ S (1 mM) and CTP (2 mM), they bound to and dissociated from the nsDNA-carpet with a stoichiometry of $\sim 1:2$ (**Figure 5A, Figure 5—figure supplement 1A**). The assembly kinetics of the carpet-bound complex was roughly the same as in the absence of CTP; however, the apparent dissociation rate constant during buffer wash was slightly but reproducibly slower by a factor of roughly two at $\sim 0.6 \text{ min}^{-1}$. When *parS_F* was included together with CTP, the rate of A₂B₄ complex assembly on the DNA-carpet increased several-fold, the binding density of the complex on the DNA-carpet reached a correspondingly higher level, and the two proteins dissociated from the DNA-carpet maintaining a $\sim 1:2$ stoichiometry with apparent dissociation rate constant similar to that in the absence of *parS_F* (**Figure 5B, Figure 5—figure supplement 1B**). When CTP was replaced by CDP in the presence of *parS_F*, although the ParB_F/ParA_F ratio remained above 2, unlike in the presence of CTP, the complex assembly rate did not increase (**Figure 5C, Figure 5—figure supplement 1C**), thus behaving similarly to the reaction in the presence of *parS_F* alone.

Next, we asked if the *parS_F* DNA fragment was incorporated in the A₂B₄ complexes assembled in its presence. The experiments in the presence of *parS_F* were repeated in the presence or absence of CTP with ParA_F (1 μM), ParB_F-Alexa647 (2 μM) and Alexa488-*parS_F* (1.1 μM), and the nsDNA-carpet-bound ratio of *parS_F* and ParB_F after 240 s sample infusion was measured (**Figure 5D**). The observed *parS_F*/(ParB_F)₂ ratio in the absence of CTP was ~ 0.2 , while in the presence of CTP, the ratio was only ~ 0.04 . Thus, whereas the assembly of the A₂B₄ complex involving CTP-ParB_F was accelerated by *parS_F*, a very small fraction of the resulting complex contained the *parS_F*-DNA fragment, indicating that *parS_F* plays a catalytic role in the activation of CTP-ParB_F and accelerated assembly of the A₂B₄ complex. This parallels the observation that a much lower concentration of *parS_F* fully activated the CTPase activity of ParB_F (**Figure 5—figure supplement 2C**) as has also been shown for ParB_{Bsu} (**Soh et al., 2019**).

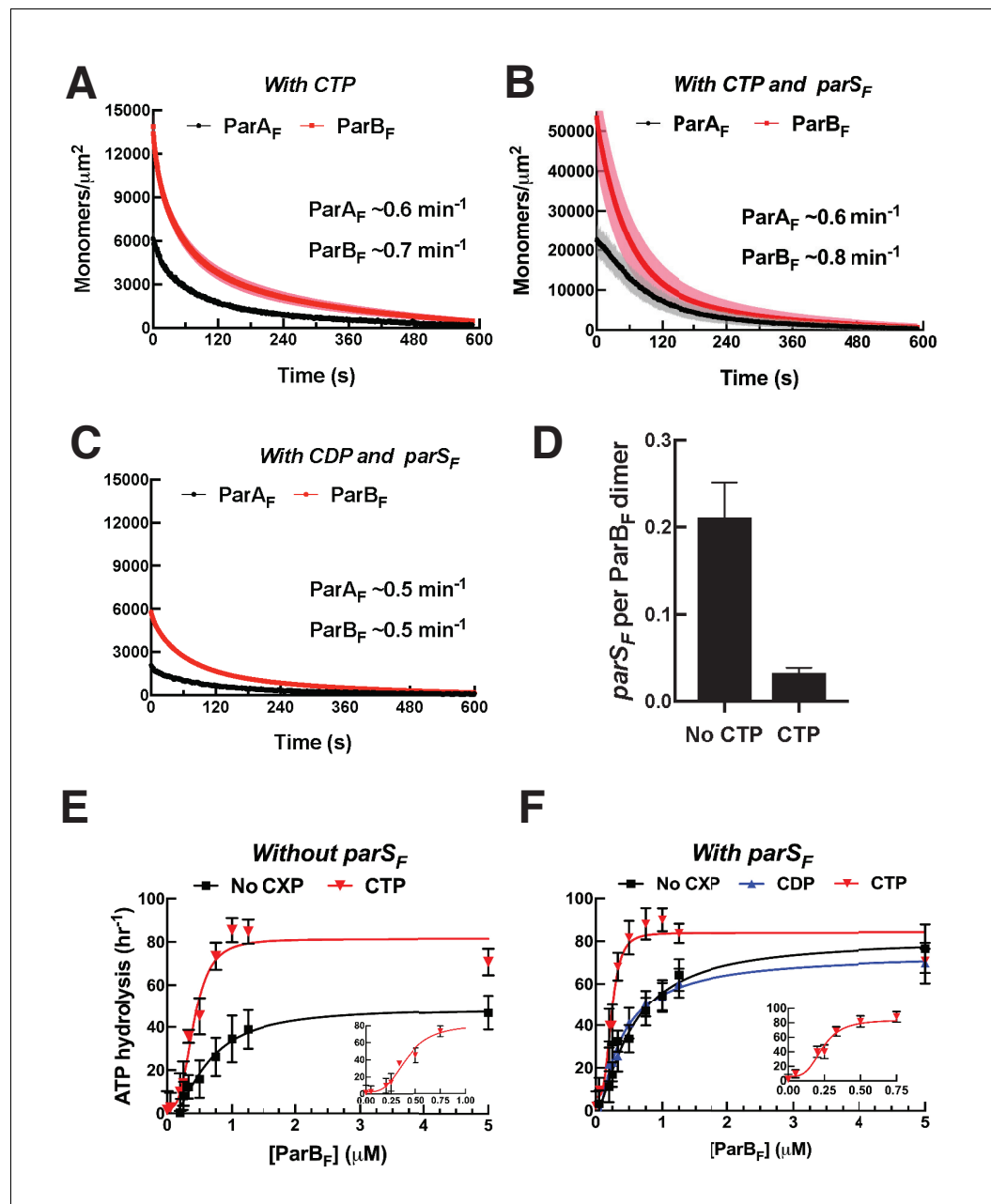


Figure 5. CTP and *parS_F* together alter interactions between ParB_F and ParA_F dimers. (A) ParA_F-eGFP (1 μM) and ParB_F-Alexa647 (2 μM) preincubated with ATP γ S and CTP (2 mM) were infused into the nsDNA-carpeted flow cell and then washed with buffer containing ATP γ S and CTP. (B) As in (A), except a 24 bp *parS_F* fragment (1.1 μM) was added to the sample mixture. (C) As in (B), except CTP was replaced by CDP. For binding curves, see **Figure 5—figure supplement 1A–C**. (D) ParA_F (1 μM), ParB_F-Alexa647 (2 μM) and Alexa488-labeled 24 bp *parS_F* fragment (1.1 μM) preincubated with ATP γ S or ATP γ S plus CTP (2 mM) were infused into the nsDNA-carpeted flow cell and after 240 s, the ratio of the carpet-bound *parS_F* fragment and ParB_F dimer was measured. (E) ParA_F-ATPase activity was measured in the presence of EcoRI-digested pBR322 DNA (60 $\mu\text{g}/\text{ml}$), different concentrations of ParB_F and either no C-nucleotide or 2 mM CTP. Inset shows data in the presence of CTP with expanded abscissa. (F) As in (E) except the reactions also contained 24 bp *parS_F* fragment (1.1-fold higher concentrations than ParB_F dimers). Inset shows data in the presence of *parS_F* and CTP with expanded abscissa. See **Figure 2** legend and **Tables 1** and **2** for additional details.

The online version of this article includes the following figure supplement(s) for figure 5:

Figure supplement 1. Binding curves for ParA_F and ParB_F with CDP or CTP associating with the DNA-carpet.

Figure 5 continued on next page

Figure 5 continued

Figure supplement 2. Nucleotide specificity and CTPase activity of ParB_F in the presence of different concentrations of CTP, in the presence or absence of *parS_F*.

ParB_F activates ParA_F-ATPase to the full extent without *parS_F* in the presence of CTP

The maximum ParB_F activation of ParA_F-ATPase in the presence of CTP, with or without *parS_F*, was comparable to that of *parS_F*-bound ParB_F in the absence of CTP (Figure 5E,F). The half-saturation concentration of ParB_F in the presence of *parS_F* and CTP was significantly lower than in the absence of CTP (~0.24 μM vs ~0.6 μM). Combined with the observation of faster assembly of the complex on the DNA-carpet, a likely possibility is that in the presence of CTP and *parS_F*, the ParB_F dimer adopts a unique state that interacts with ParA_F dimers with a higher association rate constant. We note that the ParA_F-ATPase assays in this study measured radioactive γ-phosphate release from γ-³²P-ATP, avoiding potential technical complications associated with ATPase measurements in the presence of CTP.

We next measured the ParB_F-CTPase activity to estimate the apparent K_M and k_{cat} of ParB_F for CTP hydrolysis in the presence and absence of *parS_F*. ParB_F had negligible activity for all NTPs other than CTP (Figure 5—figure supplement 2A), and the CTP hydrolysis rate increased with a hyperbolic CTP concentration dependence, which could be fit with the Michaelis–Menten equation with apparent K_M of ~8 μM and ~18 μM and maximum turnover rates of ~14 h⁻¹ and ~44 h⁻¹ in the absence and presence of *parS_F* DNA, respectively (Figure 5—figure supplement 2B). Thus, 2 mM CTP used in the experiments of Figure 5 should have remained saturating ParB_F for the duration of the reaction. Stimulation of the CTPase activity by *parS_F* exhibited a pronounced sigmoidal concentration dependence approaching saturation at ~60 nM, well below the ParB_F concentration in the reaction (0.84 μM) (Figure 5—figure supplement 2C).

During these experiments, which were prompted by a reviewer's comment, we also attempted to characterize the interaction between CDP and ParB_F, but discovered that the CDP used here contained ~2% contamination of a compound that released Pi upon incubation with ParB_F (Figure 5—figure supplement 2D). The results shown in Figure 5C and Figure 5F suggest this contamination did not strongly influence the reactions involving CDP, considering that they generally paralleled the results obtained in the absence of C-nucleotides with only minor deviations. However, this contamination prevented us from accurately determining the affinity of ParB_F for CDP.

In the presence of CTP, ParB_F condenses DNA carrying *parS_F* in cis

The recently discovered CTP and *parS*-dependent ParB conformational change appears to promote ParB *parS*-DNA binding and spreading (Soh et al., 2019), impacting ParB-DNA partition complex assembly. *In vivo*, spreading ParB forms condensed foci around *parS* sites indicating that *parS*-driven ParB spreading likely occurs *in cis*. Nonetheless, the possibility that *parS* can trigger ParB spreading *in trans* has not been tested *in vitro*. Previous studies reported DNA condensation by *B. subtilis* ParB via ParB–ParB interactions, but these studies were conducted in the absence of CTP and did not observe a strong effect of *parS* *in cis* (Graham et al., 2014; Song et al., 2017; Taylor et al., 2015). To see if *parS_F* can act *in trans* and to characterize how *parS_F* and CTP influence ParB_F-DNA interactions *in vitro*, we conducted single-molecule DNA pulling experiments employing magnetic tweezers. ParB_F at various concentrations was infused into a flow cell containing ~5 kbp DNA tethers that anchored magnetic beads to the coverslip surface (Figure 6A). The tethers contained either 12 *parS_F* consensus sequence repeats at their midpoints (*parS_F*-DNA), or no *parS_F* sequence (nsDNA). The protein sample was infused while the DNA tethers were stretched at 5 pN force, preventing DNA condensation. To allow DNA condensation by bound ParB_F molecules, the force was dropped to 0.05 pN and the tether extension was monitored for 30 s. To assess the stability of DNA condensation by ParB_F dimers, tether extension was monitored after increasing the force to 5 pN. In the absence of CTP, we only observed condensation at very high concentrations of ParB_F (>5 μM) and did not see a significant difference between *parS_F*-containing and non-specific tethers (Figure 6B inset). However, in the presence of CTP, 50 nM ParB_F robustly condensed *parS_F*-containing DNA tethers (Figure 6B purple). These condensed protein-DNA complexes resisted 5 pN extension force,

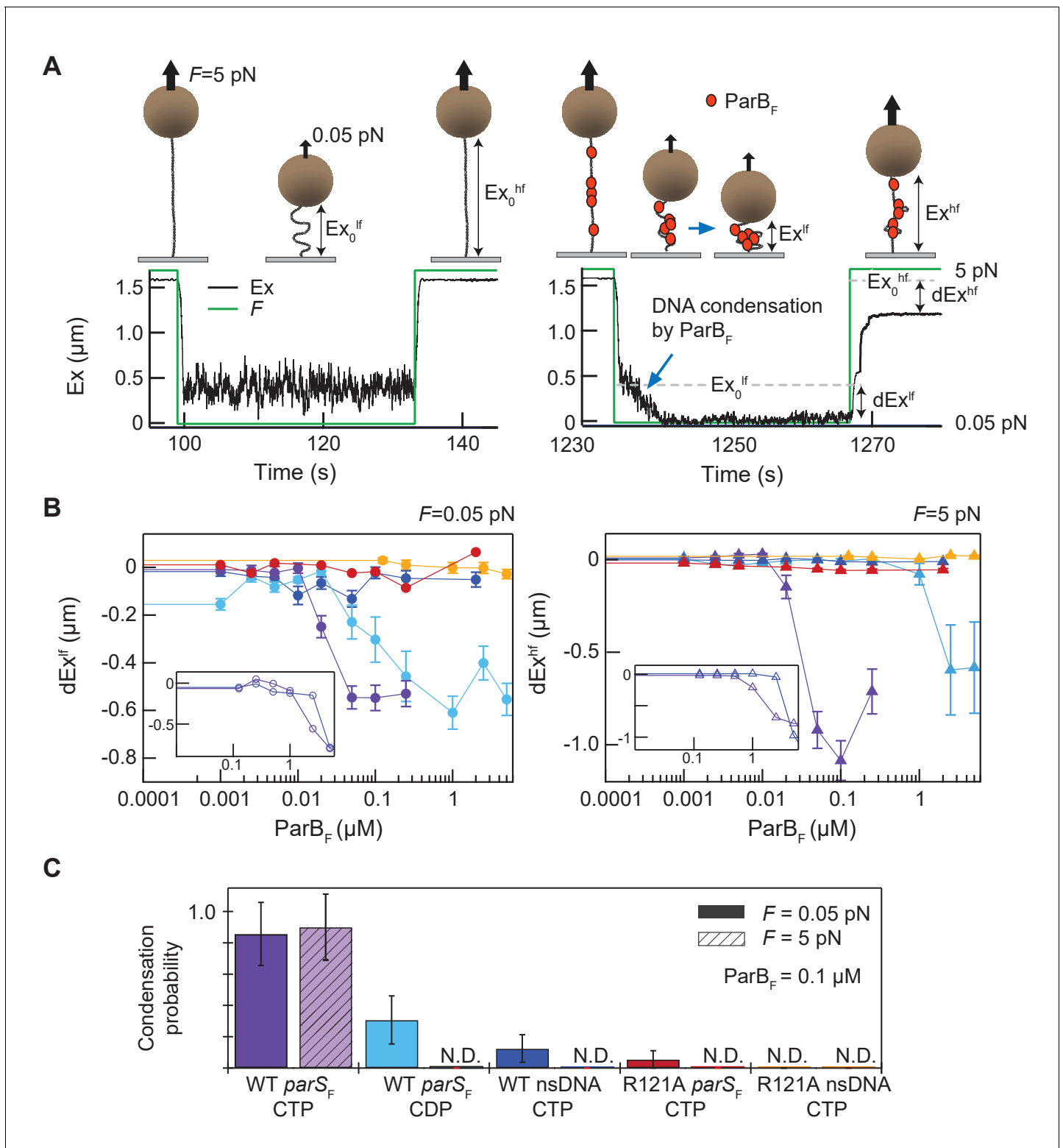


Figure 6. Magnetic tweezers measurements of $parS_F$ and CTP-dependent DNA condensation by $ParB_F$. (A) Schematic showing the magnetic tweezers DNA condensation assay. One end of a 5 kb DNA molecule is attached to the surface of a flow-cell and the free end is attached to a 1 μm magnetic bead (brown sphere). The DNA extension (Ex) was measured by tracking the bead height above the cover glass surface at two different forces; 0.05 pN (low force, l^f), and 5 pN (high force, h^f). The extent of DNA condensation was estimated from the difference in DNA extension with and without $ParB_F$. (B) Changes in extension at low force ($dEx^{lf} = Ex^{lf} - Ex_0^{lf}$), left panel, and at high force ($dEx^{hf} = Ex^{hf} - Ex_0^{hf}$), right panel, for seven different conditions plotted as a function of $ParB_F$ concentration. The extension values were the averages of the last 5 s of the extension at low force (circles) and the first 5 s of the extension at high force (triangles). (C) Condensation probability for various genotypes. The legend indicates $F = 0.05$ pN (solid bars) and $F = 5$ pN (hatched bars). $ParB_F = 0.1$ μM . N.D., Not Determined.

Figure 6 continued

s of the extension at high force (triangles). Error bars represent standard error of means (SEM). Different conditions are color coded as follows. Purple: *parS_F*-DNA tether with WT ParB_F and CTP; light blue: *parS_F*-DNA tether with WT ParB_F and CDP; dark blue: nsDNA tether with WT ParB_F and CTP; red: *parS_F*-DNA tether with ParB_F^{R121A} and CTP; orange: nsDNA tether with ParB_F^{R121A} and CTP. For comparison with condensation in the presence of CTP, dEx data of *parS_F*-DNA tether (purple) and nsDNA tether (blue) with WT ParB_F without CTP are displayed (inset, open circles for 0.05 pN, triangle for 5 pN respectively). (C) The condensation probabilities at 0.1 μM ParB_F for five different conditions at 0.05 pN and 5 pN. The condensation probability was calculated by dividing the number of DNA tethers that exhibited DNA condensation by the total number of DNA tethers for each measurement condition. Except for *parS_F*-DNA with WT ParB_F and CTP, all conditions show either minimal or negligible condensation probabilities. The different conditions are color-coded as indicated in (B), and the diagonal stripes indicates probabilities at 5 pN. Error bars represent standard error of means (SEM).

The online version of this article includes the following figure supplement(s) for figure 6:

Figure supplement 1. Stepwise de-condensation of condensed DNA tethers in the presence of CDP or CTP by tensile force: condensation observed in the presence of CDP is unstable.

Figure supplement 2. Tether condensation by ParB_F is comparable for topologically constrained (supercoilable) and unconstrained (nicked) DNA.

Figure supplement 3. DNA tethers without *parS_F* sequence are not condensed by ParB_F and *parS_F* *in trans* in the presence of CTP.

requiring many minutes at 5 pN tension to de-condense (**Figure 6—figure supplement 1A**). The slow de-condensation took place through a series of abrupt steps, which we interpret as stepwise opening of large DNA loops held by multiple ParB_F–ParB_F interactions (**Figure 6—figure supplement 1A**). Condensation was comparable for DNA molecules that were topologically constrained, i. e., could be supercoiled, or unconstrained (nicked), suggesting that condensation is not a consequence of topological changes in the DNA caused by ParB_F translocating away from *parS_F* sites (**Figure 6—figure supplement 2**). We observed some condensation events with *parS_F* containing tethers in the presence of CDP, but these events were rarer, required higher ParB_F concentrations, and were almost completely de-condensed within 5 s of raising the force to 5 pN, in stark contrast to condensation in the presence of CTP (**Figure 6B**, light blue, **Figure 6—figure supplement 1B**). Since this experiment was also carried out using CDP that contained a compound hydrolysable by ParB_F, contribution of this compound to the limited tether condensation cannot be ruled out. In contrast, ParB_F was unable to substantially condense DNA tethers lacking *parS_F* sequences, even in the presence of CTP, and rare condensation events were quickly reversed by the application of 5 pN force (**Figure 6B**, dark blue). Addition of *parS_F*-containing DNA fragments together with ParB_F and CTP did not rescue the inability to condense tethers lacking *parS_F*, indicating that *parS_F* cannot act *in trans* to promote ParB spreading and condensation of DNA molecules (**Figure 6—figure supplement 3**). Together these results indicate that *parS_F* mediates loading of multiple CTP-bound ParB_F dimers *in cis* onto the DNA-tethers and these ParB_F dimers are capable of forming DNA looping bridges likely *via* inter-dimer interactions to form a condensed partition complex-like structure. As expected, ParB_F^{R121A} bearing a mutation at the critical Box II residue in the CTPase domain was unable to condense DNA to a significant degree even with *parS_F* containing tethers (**Figure 6B**, red). We propose that stable DNA condensation by ParB_F is mediated by CTPase domain dimerization and requires both *parS_F* and CTP at moderate ParB_F concentrations (~100 nM) (**Figure 6C**).

Discussion

In this report, we characterized facets of the ParA_F–ParB_F interaction leading to the assembly of the nsDNA-bound ParA_F–ParB_F complex that is required to activate ParA_F for ATP hydrolysis and dissociation from nsDNA under the influences of *parS_F* and CTP (summarized in **Figure 7**). Our results indicate that both ParB_F binding faces of the nsDNA-bound ParA_F dimers must be occupied by a ParB_F N-terminal domain for ATPase activation (**Figures 2C–G** and **7B**). In principle, two copies of the ParB_F N-terminal domain activating a ParA_F dimer could belong to one ParB_F dimer as seen in the absence of CTP or *parS_F* (**Figures 4A,B** and **7B**, middle). However, most ParB_F dimers in partition complexes *in vivo* are likely in the CTP- and *parS_F*-activated state, spreading over a *parS_F*-proximal DNA region. CTP or *parS_F* binding alters the ParB_F dimer structure to prevent a single ParB_F dimer from providing both copies of the N-terminal domain to occupy both binding faces of a ParA_F dimer, necessitating two ParB_F dimers, each providing one N-terminal domain to a ParA_F dimer (**Figures 4C,D**, **5**, and **7B**, bottom). Strikingly, *parS_F* together with CTP significantly increased the

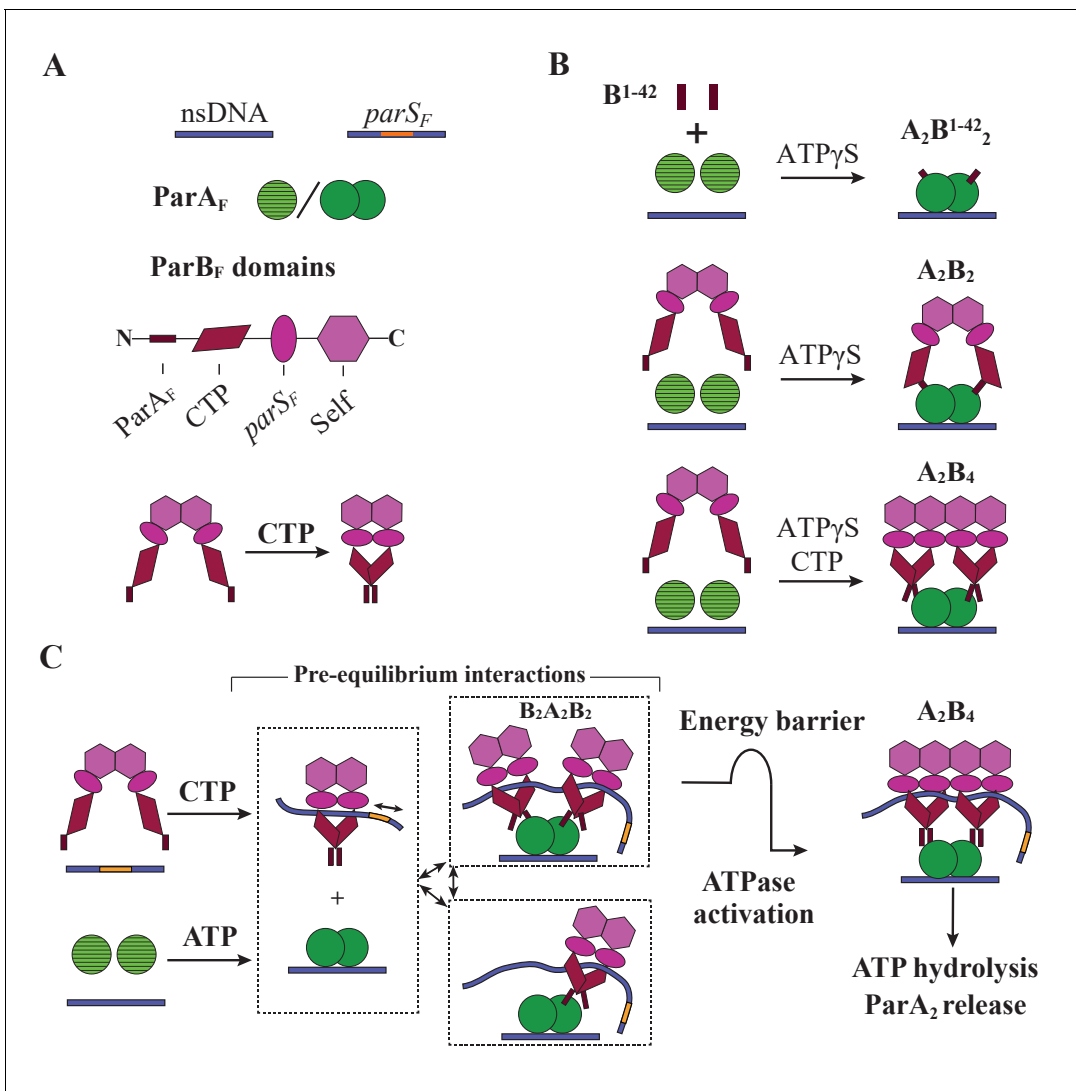


Figure 7. Cartoon of the proposed pre-ATPase-activation complexes of ParA_F and ParB_F. (A) Pictograms of nsDNA, *parS_F*-DNA, ParA_F monomer/dimer and ParB_F domains with binding ligand designations. The CTPase domains of a ParB_F dimer fold forming a single globular domain on binding CTP, bringing the two ParA_F-binding domains into close proximity. (B) ParA_F-binding domain, ParB¹⁻⁴² alone can convert ParA_F monomers to DNA-binding-competent dimers in the presence of ATPγS by forming an A₂B¹⁻⁴²₂ complex (top). ParB_F dimers in the absence of CTP convert ParA_F monomers to DNA-binding-competent dimers in the presence of ATPγS by straddling a ParA_F dimer to form an A₂B₂ complex (middle). In the presence of CTP, the close proximity of the ParA_F-binding domains of the ParB_F dimer prevents A₂B₂ complex formation and instead an A₂B₄ complex assembles on nsDNA in the presence of ATPγS (bottom). (C) In the presence of *parS_F* and CTP, ParB_F dimers load on to the *parS_F*-DNA and spread to adjacent DNA regions while adopting a state that enables faster assembly of A₂B₄ complexes. Considering the requirements for efficient partition complex motion by diffusion-ratchet mechanism based on the chemophoretic principle of force generation, we propose a significant energy barrier that slows the formation of the ATP hydrolysis-competent A₂B₄ complex. This energy barrier partially decouples ParA_F-ParB_F association-dissociation dynamics from ATP hydrolysis, which triggers ParA_F dissociation from the nucleoid.

A₂B₄ complex assembly rate on nsDNA without strongly affecting its disassembly rate. Although we have not analyzed the full kinetic details of the process that leads to ATPase activation by ParB_F, we propose that a moderately slow transition separates formation of the ATPase-activated A₂B₄ complex from the rapidly reversible ParA_F-ParB_F interaction processes. Such a local slow step would partially decouple the reversible ParA_F-ParB_F interaction dynamics from the irreversible ATP hydrolysis, thereby promoting dynamic interactions between the nucleoid and partition complex that facilitate partitioning via the diffusion-ratchet mechanism as elaborated below.

The clearest indication that both ParB_F-interacting faces of the nsDNA-bound ParA_F dimer must be occupied by the N-terminal domain of ParB_F for ATPase activation came from experiments using

artificial ParB_F constructs. We showed that monomeric ParB_F¹⁻⁴² stimulates ParA_F ATPase with a clear sigmoidal concentration dependence, indicating that one molecule of ParB_F¹⁻⁴² binding to one side of a ParA_F dimer cannot fully activate the ParA_F ATPase (**Figure 2F**). When ATP hydrolysis was blocked by using non-hydrolysable ATPγS, ParB_F¹⁻⁴²-mCherry formed an equimolar complex with ParA_F (**Figure 2C-E**). Thus, the ParA_F forms a complex with ParB_F¹⁻⁴²-mCherry bound at both ParB_F-interacting faces of the ParA_F dimer prior to ATP hydrolysis (**Figure 7B**; top). Consistently, an artificially dimeric ParB_F¹⁻⁴² construct, ParB_F¹⁻⁴²-mCherry-EcoRI^{E111Q}, efficiently activated ParA_F-ATPase with hyperbolic concentration dependence (**Figure 2G**).

In the absence of CTP or *parS_F*, the ParB_F dimer is held together by the C-terminal self-dimerization domain (**Figure 7A**, bottom) with dimerization K_D of ~19 nM (**Figure 4—figure supplement 1**). In this state, the N-terminal halves of the monomers are thought to be separate from each other according to the SAXS envelope of the structure (**Chen et al., 2015**; also see **Figure 2—figure supplement 3B**). Thus, one dimer could straddle a ParA_F dimer with each N-terminal ParA_F-interaction domain interacting with one of the two faces of a ParA_F dimer (**Figure 7B**, middle).

In contrast, when bound by CTP the CTPase domains in a ParB_F dimer fold to form a single globular domain (**Figure 7A**, bottom) (**Soh et al., 2019**; see **Figure 2—figure supplement 3C**). The two ParA_F-interaction domains emanating from this dimeric domain are unlikely to reach both sides of a ParA_F dimer, necessitating an A₂B₄ complex for ATPase activation (**Figure 7B**, bottom). In theory, it is possible that a chain of (A₂B₂)_n might form, but the 1:2 protein stoichiometry observed in the presence of ATPγS indicates such a configuration is unfavored. A₂B₄ complexes formed in the presence of CTP and *parS_F* DNA fragments contained almost no *parS_F* DNA fragments (**Figure 5D**). This is consistent with the notion that after binding *parS_F*, CTP-ParB_F dimers convert to a low *parS_F*-affinity state while remaining topologically bound to the DNA and spreading to surrounding DNA regions (**Soh et al., 2019**). The A₂B₄ complex formed in the presence of *parS_F* DNA fragments, even without CTP, contained significantly less than a stoichiometric amount of *parS_F* fragment (**Figure 5D**). This suggests that association with nsDNA-bound ParA_F dimer lowers the affinity of ParB_F for *parS_F*, perhaps shifting the structure closer toward *parS_F*-activated ParB_F-CTP.

The ParB:ParA stoichiometry change from 1:1 to 2:1 caused by *parS_F* (**Figure 4C,D**) did not occur with the Box II mutant ParB_F^{R121A} (**Figure 4—figure supplement 2**). It is possible that when a ParB_F dimer binds *parS_F*, the adjacent CTPase domains of the two monomers adopt a mutually interacting folded state akin to the CTP-bound state even without CTP, promoting a Box II dependent dimerized domain structure. This may disfavor formation of the A₂B₂ complex, favoring the A₂B₄ complex that was observed.

All the A₂B₂ and A₂B₄ complexes we observed in the presence of ATPγS dissociated from nsDNA more slowly ($k_{off} = 0.5-1 \text{ min}^{-1}$; **Source data 1**) compared to ParA_F in the absence of ParB_F (~6 min^{-1} ; **Figure 2B**). For the case of monomeric ParB_F¹⁻⁴², which dissociated from ParA_F more rapidly, the presence of 10 μM ParB_F¹⁻⁴² in the wash buffer restored the low apparent nsDNA dissociation rate constant of the complex (**Figure 2E**). Nevertheless, ParA_F dimers in these complexes appear to be primed for further conformational change toward less stably DNA-associated state. Upon dissociation of ParB_F¹⁻⁴² from the A₂B₂¹⁻⁴² complex, ParA_F dissociated from the DNA-carpet within a second or so, much faster than the ATPγS-ParA_F-dimer that has not yet formed a A₂B₂ or A₂B₄ complex (**Figures 2D and 3B**).

Our single-molecule DNA condensation measurements indicate that CTP-bound ParB_F dimers are activated by contacting *parS_F* to load *in cis* onto the *parS_F*-carrying DNA in numbers exceeding the copy number of the *parS_F*-consensus sequence (ParB spreading) as shown by others for chromosomal ParBs (**Jalal et al., 2020**; **Soh et al., 2019**), and condense the DNA forming an *in vivo* partition complex-like structure (**Figure 6**). Although the magnetic tweezers instrument used in this study did not allow direct measurement of the number of ParB_F molecules contained in the condensed DNA, the large number of de-condensation steps observed when high tension was applied is consistent with the presence of a large number of ParB_F dimers in the condensed DNA (**Figure 6, Figure 6—figure supplement 1A**). CDP failed to support efficient condensation of *parS_F*-carrying DNA by ParB_F and the limited condensation observed, which could be due to the contaminating material in the CDP used, was disrupted far more readily than CTP-supported condensates (**Figure 6, Figure 6—figure supplement 1B**). Our results show that DNA-condensation is caused by ParB_F-ParB_F interactions forming DNA-looping bridges without requiring other protein factors. Combined with evidence indicating that *parS_F*-activated ParB_F-CTP adopts a unique conformational state

(Soh et al., 2019), we favor the view that DNA-bridging capability, mediated by inter-dimer ParB_F interaction, is another attribute of this ParB_F state.

Our observation indicates that the state of ParB_F discussed above is maintained after release from *parS_F*-containing DNA. ParB_F associates with nsDNA-bound ParA_F dimers forming the A₂B₄ complex with a faster apparent assembly rate in the presence of *parS_F* and CTP together than with either CTP or *parS_F* alone. This observation is consistent with the decreased half-saturation concentration in the ATPase activation assay (Figure 5F, Table 2). According to the sliding clamp model of spreading ParB–CTP dimers proposed by Soh et al., 2019, ParB–CTP dimers loaded onto a short *parS_F* DNA fragments would quickly slide off the DNA as shown by Jalal et al., 2020. Since our ATPase activation assay and the DNA-carpet-bound A₂B₄ complex assay in the presence of CTP and *parS_F* were done using a short linear *parS_F* DNA fragment, the *parS_F*-activated state of the ParB–CTP dimers we described in this study must remain in this ‘activated’ state for an extended period after sliding off the *parS_F* fragment. Accordingly, the A₂B₄ complexes bound to the DNA-carpet in the presence of CTP, ATP_γS and *parS_F* fragments contained almost no *parS_F* fragments (Figure 5D). Thus, *parS_F* acts as a catalyst to convert ParB–CTP dimers from a pre-activation state to an activated state capable of faster A₂B₄ complex assembly. This notion is also consistent with the observation that significantly less than a stoichiometric concentration of *parS* DNA relative to ParB is sufficient for full activation of the ParB CTPase (Figure 5—figure supplement 2C; Soh et al., 2019). Although the ParB_F dimers in this activated state failed to load efficiently onto DNA lacking *parS_F* sequences *in trans* (Figure 6—figure supplement 3), in the absence of contrary evidence, the parsimonious assumption is that this ParB_F dimer retains the conformation of spreading ParB_F dimers that remain loaded on the *parS_F*-containing DNA *in cis*. Thus, we propose that the functional properties of ParB_F we observed in the presence of CTP and *parS_F*, both in facilitating assembly of A₂B₄ complexes and in activating ParA_F-ATPase, reflect those of the majority of ParB_F dimers in partition complexes *in vivo*.

Our study, together with previous studies, indicates that the ATP turnover rates of ParABS systems are slow because of multiple, slow kinetic steps. These slow steps are strategically placed in the reaction pathway in order to tune the system and drive the motion of the partition complex through the diffusion-ratchet mechanism (Sugawara and Kaneko, 2011; Vecchiarelli et al., 2010). Even at saturating concentrations of ParB_F in the *parS_F*-activated CTP-bound state, the maximum ATP turnover rate of ParA_F remained modest (~80 ATP/ParA_F-monomer/hour; Figure 5). The slow reactivation of ParA nucleoid binding after ATP hydrolysis likely dominates the overall ATPase cycle time (Vecchiarelli et al., 2010). The presence of a large fraction of ParA_F in the DNA-unbound state during the steady-state ATPase assay was evidenced by the fact that the half-saturation concentration of ParB_F (in the presence of CTP and *parS_F*) forming the A₂B₄ complex was ~0.2 μM, while the total ParA_F concentration was 1 μM, suggesting less than ~20% of ParA_F was in the nsDNA-bound state ready to interact with ParB_F. *In vivo* the reactivation rate is likely lower since nucleoid-bound ParA is only fully activated on encountering the partition complex, which lowers the concentration of ParA in the cytosol waiting to be reactivated. The lower precursor concentration slows the nucleoid rebinding rate of ParA non-linearly because reactivation involves a relatively fast nucleotide-dependent reversible ParA dimerization with apparent K_D of ~2 μM, followed by a slow conformational step. This makes the process dimerization-limited at lower precursor ParA concentrations according to the study of ParA_{P1} (Vecchiarelli et al., 2010). Whereas this slow ParA reactivation and rebinding process, which allows the maintenance of the nucleoid-bound ParA concentration gradient (Hu et al., 2017), is a critical element of chemophoresis driven motility, the rate of ParA-ATPase activation by ParB is another important factor. In particular, efficient chemophoresis force generation relies on ParA_F–ParB_F interactions achieving a local quasi-equilibrium prior to ATP hydrolysis (Sugawara and Kaneko, 2011). Therefore, we speculate that there is a significant energy barrier associated with the conformational transition of a ParA_F–ParB_F complex to achieve ATPase activation (Figure 7C). The resulting local time delay, in addition to the fact that two ParB dimers are required to bind a ParA dimer to activate its ATPase, would partially decouple the pre-ATP hydrolysis ParA_F–ParB_F reversible interaction steps from the ATP hydrolysis step. This delay would in turn permit ParB–ParA binding to approach local quasi-equilibrium, increasing the efficiency of ParA distribution gradient sensing and motive force generation by the partition complex. In addition, this slow activation step would prevent possible over-depletion of the local nucleoid-bound ParA_F as the partition complex establishes the ParA_F depletion zone.

Disassembly of the ATP-bound A_2B_4 complex might be slow prior to ATP hydrolysis considering the stability of the complexes in the presence of ATP γ S. Thus, we propose the energy barrier postulated above is positioned immediately prior to formation of this complex rather than between this complex assembly and ATP hydrolysis. A slow step after formation of the stable complex would prolong the lifetime of the link between the nucleoid and the partition complex impeding partition complex motion without permitting the reversible ParA_F–ParB_F interaction to approach equilibrium. We consider this conformational transition is likely the step synergistically accelerated by CTP and *parS_F*. We note that CTP-activated ParB_F stimulates ParA_F ATPase with sigmoidal concentration dependence (Figure 5E,F, Table 2), suggesting two ParB_F dimers separately bind a ParA_F dimer during a pre-equilibrium binding phase, forming a transient $B_2A_2B_2$ complex. We imagine the slow conformational step proposed here might be assisted by the property of the CTP/*parS_F*-activated ParB_F dimers that promotes inter-dimer interactions as suggested by the magnetic-tweezers experiments, stabilizing the interaction between the two ParB_F dimers within a complex, depicted as conversion of $B_2A_2B_2$ complex to A_2B_4 complex in Figure 7C. This might explain the higher assembly rate and stability of the complex formed with *parS_F*-activated ParB_F-CTP. Yet, CTP and *parS_F* DNA do not significantly increase the ATP turnover rate of $\sim 80\text{ h}^{-1}$, indicating that the proposed kinetic delay time must be a small fraction of the ATPase cycle time ($\sim 45\text{ s}$), for which we believe the rate limiting step resides in the reactivation process of ParA for nsDNA binding after ATP hydrolysis (Vecchiarelli et al., 2010). Assembly of the $A_2B^{1-42}_2$ complex perhaps does not experience this time delay due to fewer steric constraints, but ParB_F¹⁻⁴² dissociates more readily compared to full-length ParB_F. If two CTP-bound and *parS_F*-activated ParB_F dimers independently associating with a nucleoid-bound ParA_F-ATP dimer is important for efficient partition complex motive force generation by the chemophoretic principle as proposed above, one might be able to design a mutant ParB_F that can activate ParA_F-ATPase by forming an A_2B_2 complex even in the presence of CTP, which would significantly affect plasmid partition efficiency. Efforts to generate such ParB_F mutants are currently under way.

This study demonstrates how *parS_F*, along with CTP, has wide-reaching roles in the F-plasmid Par-ABS system; not only in ParB_F's ability to spread from *parS_F* and promote ParB_F–ParB_F interactions for partition complex compaction, but also in ParB_F dimer interactions with ParA_F. However, we still need to investigate how the ParB_F CTPase activity is impacted by *parS_F* in different states of the ParB_F–*parS_F* complex and its interaction with the ParA_F-DNA complex. More generally, in order to understand how the system is orchestrated to achieve system dynamics that result in robust plasmid segregation, improved understanding of the microscopic kinetic parameters is essential. Many details of the system dynamics still remain to be addressed to understand the full picture of the Par-ABS partition mechanism.

Materials and methods

Key resources table

Reagent type (species) or resource	Designation	Source or reference	Identifiers	Additional information
Strain, strain background (<i>Escherichia coli</i>)	BL21 DE3 AI	Invitrogen	C607003	Protein expression strain
Recombinant DNA reagent	pET11a	EMD Millipore	9436	Protein expression vector
Recombinant DNA reagent	pET28a- <i>parS_F</i>	This work		Tether DNA PCR template
Recombinant DNA reagent	pET28a	EMD Millipore	69865	Tether DNA PCR template
Recombinant DNA reagent	pBlueScript II KS(+)	Agilent	212207	Tether DNA PCR template

Continued on next page

Continued

Reagent type (species) or resource	Designation	Source or reference	Identifiers	Additional information
Recombinant DNA reagent	pX7	Vecchiarelli et al., 2013		ParA _F overexpression plasmid
Recombinant DNA reagent	pX2	Vecchiarelli et al., 2013		ParA _F -eGFP overexpression plasmid
Recombinant DNA reagent	pX8	Vecchiarelli et al., 2013		ParB _F overexpression plasmid
Recombinant DNA reagent	pET11a-ParB _F ^{R121A}	This work		ParB _F ^{R121} overexpression plasmid
Recombinant DNA reagent	pET11a-ParB _F ¹⁻⁴² -mCherry	This work		ParB _F ¹⁻⁴² -mCherry overexpression plasmid
Recombinant DNA reagent	pET11a-ParB _F ^{1-42 R36A} -mCherry	This work		ParB _F ^{1-42 R36A} -mCherry overexpression plasmid
Recombinant DNA reagent	pET11a-ParB _F ¹⁻⁴² -mCherry-EcoRI ^{E111Q}	This work		ParB _F ¹⁻⁴² -mCherry-EcoRI ^{E111Q} overexpression plasmid
Sequence-based reagent	parS _F DNA	This work		5'-AGTCTGGGACCA CGGTCCCACTCG
Sequence-based reagent	parS _F DNA Alexa 488	This work		5'-Alexa488-(HNS)- AGTCTGGGACCAC GGTCCCACTCG
Sequence-based reagent	parS _F DNA complement strand	This work		5'-CGAGTGGGACC GTGGTCCCACTCG
Sequence-based reagent	Scrambled seq DNA	This work		5'-AGTCTGCAGCTAC TATACCACTCG
Sequence-based reagent	Scrambled seq DNA complement strand	This work		5'-CGAGTGGTATAGT AGCTGCAGACT
Sequence-based reagent	EcoR1 sequence + strand	This work		5'-GAATTCGAGTGGG ACCGTGGTCCCAGTCT GATTATCAGACCGAGA ATCAAGTTGGGACC GTGGTCCCAAGAGAAT
Sequence-based reagent	EcoR1 sequence - strand	This work		5'-ATTCTCTGGGACCAC GGTCCCAACTTGAATTC TCGGTCTGATAATCAGA CTGGGACCACGGTCCC ACTCGGAATTC
Sequence-based reagent	5 kb DNA primer1	Seol and Neuman, 2011		5'- GCTGGGTCTCGGTT GTTCCCTTTAGTGAG GGTTAATTG
Sequence-based reagent	5 kb DNA primer2	Seol and Neuman, 2011		5'- GCTGGGTCTCGTG GTTCCCTTTAGTG AGGGTTAATTG
Sequence-based reagent	DNA handle primer1	Seol and Neuman, 2011		5'- GGACCTGCTTTCG TTGTGGCGTAATC ATGGTCATAG
Sequence-based reagent	DNA handle primer2	Seol and Neuman, 2011		5'- GGGTCTCGTGG TTTATAGTCTG TCGGGTTTC
Peptide, recombinant protein	ParB _F ¹⁻⁴²	This work		MKRAPVIPKHTLNT QPVEDTSLSTPAAP MVDSLIARVGMAR
Peptide, recombinant protein	ParB _F ^{1-42 R36A}	This work		MKRAPVIPKHTLNTQ PVEDTSLSTPAAPM VDSLIAAVGMAR

Continued on next page

Continued

Reagent type (species) or resource	Designation	Source or reference	Identifiers	Additional information
Chemical compound, drug	ATP	Millipore-Sigma	A2383	
Chemical compound, drug	GTP	Millipore-Sigma	G8877	
Chemical compound, drug	UTP	Thermo Scientific	J23160	
Chemical compound, drug	CTP	Millipore-Sigma	C1506	
Chemical compound, drug	CDP	Millipore-Sigma	C9755	2–3% possible contamination of ParB _F -CTPase substrate detected
Chemical compound, drug	$\gamma^{32}\text{P}$ -ATP	Perkin-Elmer	NEG002A250UC	
Chemical compound, drug	Dynabeads MyOne Streptavidin T1	Invitrogen	65601	
Chemical compound, drug	Alexa Fluor 488 C5 Maleimide	Thermo Fisher	A10254	
Chemical compound, drug	Alexa Fluor 594 C5 Maleimide	Thermo Fisher	A10256	
Chemical compound, drug	Alexa Fluor 647 C2 Maleimide	Thermo Fisher	A20347	
Chemical compound, drug	Antifoam Y-40 emulsion	Sigma	A5758	
Chemical compound, drug	EDTA-free Sigmafast protease inhibitor cocktail tablet	Sigma	S8830	
Chemical compound, drug	DOPC	Avanti polar lipids	850375C	
Chemical compound, drug	DOPE-Biotin	Avanti polar lipids	850149P	
Chemical compound, drug	Biotin-14-dCTP	Thermo Fisher	19518018	
Chemical compound, drug	Biotin-16-dUTP	Roche	11093070910	
Chemical compound, drug	Digoxigenin-11-dUTP	Roche	11093088910	
Commercial assay or kit	EnzChek Phosphate assay kit	Thermo Fisher	E6646	

Continued on next page

Continued

Reagent type (species) or resource	Designation	Source or reference	Identifiers	Additional information
Software, algorithm	Prism 8	GraphPad	Prism 8	Used for curve fitting, and fitting parameters and their error estimation.
Software, algorithm	Igro Pro 7	Wavemetrics	Igro Pro	Used for single molecule data analysis.
Software, algorithm	LabVIEW	National Instruments	LabView NXG Full	Used for instrumental control in single molecule experiments.
Software, algorithm	Metamorph 7	Molecular Devices	Metamorph 7	Used for TIRF microscope data acquisition.
Software, algorithm	ImageJ/Fiji	National Institutes of Health	ImageJ	Used for TIRF microscope image analysis.
Other (Instrument)	Prism type TIRF microscope	In house <i>Ivanov and Mizuuchi, 2010;</i> <i>Vecchiarelli et al., 2013</i>		Used for ParAF-ParBF complex assembly-disassembly experiments.
Other (Instrument)	Magnetic tweezers	In house <i>Seol and Neuman, 2011</i> and <i>Seol et al., 2016</i>		Used for taking single molecule measurements of enzyme binding on 5 kb DNA.
Other (Instrument)	Plate reader	BMG Labtech	Clariostar Plus	Used for FRET-based ParBF dimerization K_D and CTP hydrolysis assays using EnzChek Phosphate assay kit

Plasmids and constructs for protein expression

All expression open-reading frames were synthesized and subcloned into pET11a (Genscript). ParA_F, ParA_F-eGFP, ParB_F, ParB_F^{R121}, ParB_F¹⁻⁴²-mCherry, ParB_F^{1-42 R36A}-mCherry, and ParB_F¹⁻⁴²-mCherry-EcoRI^{E111Q} constructs were made with a hexa-histidine tag on their C-terminus. Protein fusions were made with a SGGG linker between fused domains, with exception of ParB_F¹⁻⁴²-mCherry-EcoRI^{E111Q}, which had a 4× (SGGG) linker between ParB_F¹⁻⁴² and mCherry. ParB_F¹⁻⁴² and ParB_F^{1-42 R36A} were synthesized *de novo* (Genscript).

Oligonucleotides

The 24 bp double-stranded DNA fragments containing the *parS_F* consensus sequence and a scrambled sequence used in this study were as follows: 5'-AGT CTG GGA CCA CGG TCC CAC TCG; 5' - AGT CTG CAG CTA CTA TAC CAC TCG, respectively, and their complements. The fluorescently labeled *parS_F* substrate was synthesized with Alexa-488 NHS coupled with the 5' of the forward strand by the manufacturer (IDT).

Protein purification and fluorescent labeling

For expression of proteins 5 ml of an overnight culture of BL21 DE3 AI (Invitrogen), *E. coli* cells transformed with the desired plasmid were inoculated into 500 ml Terrific Broth (Teknova) supplemented with 100 µg/ml carbenicillin, antifoam Y-40 emulsion (Sigma), 1 g/l NaCl, 0.7 g/l Na₂SO₄, 2.6 g/l NH₄Cl, and 0.24 g/l MgSO₄. The cultures were incubated at 37°C in 2.5 l Fernbach flasks and shaken at 120 rpm until they reached an OD₆₀₀ of 1.8. Cultures were chilled on ice before they were induced by the addition of 1 mM IPTG and 0.2% L-arabinose. Following induction, cultures were incubated at 16°C for 16 hr, and cells were harvested by centrifugation at 6000 × g for 15 min at 4°C. Cell pellets were frozen in liquid nitrogen and stored at -80°C.

Frozen cells were thawed and resuspended to a density of 1 g cell pellet/10 ml in lysis buffer (ParA_F, ParA_F-eGFP, and ParB_F¹⁻⁴²-mCherry-EcoRI^{E111Q}: 25 mM Tris-HCl pH 8, 1 M NaCl, 20 mM imidazole, 2 mM β-mercaptoethanol, 10% glycerol; ParB_F and ParB_F^{R121A}: 10 mM Sodium Phosphate

buffer pH 7, 1 M NaCl, 20 mM Imidazole, 2 mM β -mercaptoethanol, 10% glycerol; ParB_F¹⁻⁴²-mCherry and ParB_F^{1-42/R36A}-mCherry: 25 mM HEPES.KOH pH 7.5, 150 mM NaCl, 6 M guanidinium chloride, 20 mM Imidazole, 2 mM β -mercaptoethanol, 10% glycerol) containing EDTA-free Sigmafast protease inhibitor cocktail tablet (Sigma) using a homogenizer. Lysozyme and benzonase (Sigma) were added to a concentration of 1 mg/ml and 50 u/ml, respectively, and the cells were lysed via a microfluidizer. Cell debris were pelleted by centrifugation at $142,000 \times g$ for 45 min at 4°C, and the supernatant passed through a 0.22 μ m filter.

Lysate was loaded on to a 5 ml HisTrap HP cassette (GE Healthcare) equilibrated in lysis buffer. The cassette was then washed with 10 column volumes of lysis buffer followed by 10 column volumes HisTrap buffer (as lysis buffer without guanidinium hydrochloride and with the following NaCl concentrations: ParA_F proteins, 200 mM; ParB_F proteins, 150 mM), and the protein eluted with a gradient from 20 to 500 mM imidazole over 10 column volumes using an AKTA Pure (GE Healthcare).

All proteins except ParB_F¹⁻⁴²-mCherry and ParB_F^{1-42 R36A}-mCherry were then subjected to ion-exchange chromatography. The peak fractions from the HisTrap column were pooled and slowly diluted whilst stirring with a Mono Q/S-buffer (as lysis buffer without imidazole or NaCl, but with 0.1 mM EDTA pH 8) until the conductivity of the sample was as follows: 18 mS/cm for ParA_F proteins, 5 mS/cm for ParB_F¹⁻⁴²-mCherry-EcoRI^{E111Q}, and 15 mS/cm for all other ParB_F proteins. The conductivity of the samples was monitored using a conductivity meter (Hanna). The sample was loaded onto either a 1 ml Mono Q (ParA_F proteins and ParB_F¹⁻⁴²-mCherry-EcoRI^{E111Q}) or Mono S (other ParB_F proteins) 5/50 GL ion exchange column (GE Healthcare) pre-equilibrated with Mono Q/S-buffer containing a NaCl concentration to match the conductivity of the sample. The column was then washed with 10 column volumes of Mono Q/S-buffer + NaCl. The protein was eluted with a gradient up to 500 mM NaCl over 10 column volumes.

Finally, all protein samples were purified by size-exclusion chromatography. The peak fractions from the previous column were pooled and diluted 50:50 with concentration buffer (25 mM HEPES.KOH pH 7.5, 2 M NaCl, 2 mM β -mercaptoethanol, 10% glycerol) and concentrated to ~2 ml using a Centriprep 10 kDa spin concentrator (Millipore). The sample was then injected onto an S200 16/600 size exclusion column (GE Healthcare) pre-equilibrated in gel filtration buffer (25 mM HEPES-KOH pH 7.5, 0.1 mM EDTA pH 8, 0.5 mM TCEP and 10% glycerol with 600 mM KCl for ParA_F proteins and 150 mM KCl for ParB_F proteins). Peak fractions were then pooled and concentrated to ~100 μ M (~5–10 mg/ml) as determined by UV 280 nm absorbance before being aliquoted, frozen in liquid nitrogen, and stored at -80°C. Protein aliquots were used once and not subjected to freeze-thaw cycles.

To produce fluorescently labeled ParB_F and ParB_F^{R121A}, ParB_F protein was buffer exchanged into gel filtration buffer without reducing agent and incubated with a twofold molar excess of Alexa Fluor 647 C2 Maleimide (Thermo Fisher) for 30 min at room temperature. The reaction was then quenched by the addition of DTT to a final concentration of 10 mM. The protein solution was then filtered through a 0.22 μ m filter and free dye removed by buffer exchange into gel filtration buffer in Amicon ultra 10 kDa spin concentrator (Millipore). The extent of labeling was estimated based on absorbance at 280 and 647 nm.

Assaying contaminating activities in the protein preparations

Proteins purified by the above protocol had no significant DNA endonuclease activity. After 16 hr incubation of supercoiled pBR322 with 2 μ M ParA_F and/or 10 μ M ParB_F at 37°C in ATPase buffer (see below), no linear DNA was observed and less than 10% of the supercoiled plasmid was converted to a nicked-circular form. The contaminating ATPase activity for all ParB_F proteins was less than 2 mol ATP per mol ParB_F per hour, as determined by the ATPase assay protocol detailed below.

ATPase activity assays

Steady-state ATPase activity was measured as described (Vecchiarelli *et al.*, 2016) with modifications. ATP to be used for ATPase activity assays was purified after diluting 20 μ Ci ATP γ -P³² (Perkin-Elmer) in 100 μ l of 100 mM unlabeled ATP (Sigma) by passing through a 3 ml P2 resin size-exclusion column equilibrated with a buffer containing 50 mM HEPES.KOH pH 7.5, 150 mM KCl, and 0.1 mM EDTA. The purity of fractions was determined by TLC. One microliter of each fraction was spotted

on to a 10 × 8 cm piece of TLC PEI Cellulose F paper (Millipore) 1 cm above the bottom of the paper and developed for 10 min using 400 mM NaH₂PO₄ pH 3.6 as the solvent. The fractions containing the minimum contamination of P³²-Pi were pooled and their concentration determined by spectrometry before storage at −20°C.

ParA_F ATPase activity was measured in the presence of the combinations and concentrations of proteins and DNA cofactors specified in the main text in ATPase buffer (50 mM HEPES-KOH pH 7.5, 150 mM KCl, 5 mM MgCl₂, 0.5 mM TCEP, and 1 mM ATP γ-P³²). Reactions were incubated at 37°C for 4 hr and stopped by the addition of an equal volume of 1 M formic acid. The increase of P³²-Pi was measured by TLC using PEI Cellulose F paper as detailed above.

ParB_F NTPase activity assays

Steady-state ParB_F CTPase activity was measured in CTPase buffer containing 50 mM Tris-HCl pH 7.5, 100 mM NaCl, 2 mM MgCl₂, 1 mM DTT, 100 μg/ml BSA, 200 μM MESG (EnzChek probe), 1 U/ml of purine nucleotide phosphorylase, and ParB_F, parS_F DNA, and CTP at concentrations specified in the figure, following the protocol of the supplier of the EnzChek phosphate assay kit (Thermo-Fisher). Reactions were typically repeated three times using 96-well microtiter plates and the 360 nm absorption signal increase was monitored at 0.5–1 min intervals using Clariostar Plus plate reader (BMG Labtech). The absorption signal increase after subtraction of background time course in the absence of enzyme was converted to released Pi concentration increase based on phosphate titration measurements. The CTP hydrolysis rate was calculated from the initial slope of the time course curve, which typically started after ~7 min deadtime for the plate setting up. Substrate specificity was examined comparing Pi release from four ribonucleoside triphosphates. Attempt to examine inhibition of the CTPase activity by CDP or to detect CDP binding to ParB_F was postponed when the CDP used in this study was found to release Pi upon incubation with ParB_F. CDP obtained from two additional suppliers also generated similar quantities of Pi upon incubation with ParB_F.

TIRF microscopy

The general design of the TIRF microscopy setup was essentially as previously described (Ivanov and Mizuuchi, 2010; Vecchiarelli et al., 2013). A prism-type TIRFM system was built around an Eclipse Ti microscope (Nikon) with a 40× objective (S Fluor, 40×/1.30 oil, Nikon) and two-color images captured by an Andor DU-897E camera through a dxcr630 insert DualView (Photometrics) with the following settings: 3 MHz digitizer (gray scale); 5.2 pre-amplifier gain, 2 MHz vertical shift speed; +one vertical clock range; electron-multiplying gain 30; EM CCD temperature set at −90°C; baseline clamp ON; and exposure time 100 ms.

The excitation for ParA_F-eGFP and Alexa647-ParB_F were provided by a 488 nm diode-pumped solid-state laser (Sapphire, Coherent) and a 633 nm HeNe laser (Research Electro-Optics), respectively. The TIRF illumination had an elliptical Gaussian shape in the field of view therefore intensity data for DNA-carpet-bound ParA_F-eGFP and Alexa647-ParB_F signals were taken at or near the middle of the illumination profile.

Movies were acquired using Metamorph 7 (Molecular Devices) and transferred to ImageJ (National Institutes of Health) for analysis.

Flow cells were assembled using fused silica microscope slides with pre-drilled inlet/outlet ports (Esco products), #1 glass cover slips (24 × 50 mm, Thermo Fisher) and 0.001'-thick acrylic transfer tape (3M). The fused silica slide was cleaned by soaking overnight in a solution of Nochromix (Sigma)-sulfuric acid, followed by extensive rinsing with de-ionized water, drying by blowing nitrogen gas, followed by oxygen plasma treatment (South Bay Technology Inc). The Y-shaped flow path pattern was cut out of the transfer tape using a laser cutter before the flow cell assembly. Nanoports (Idex) were attached to the fused silica slide for the inlet and outlet tube connections using Norland Optical Adhesive (Thorlabs), cured by 365 nm UV light. The assembled flow cells were then baked at 80°C with gentle compression for 2 hr.

To assemble a DNA-carpet in a flow cell, small unilamellar vesicles (SUVs) of 1,2-dioleoyl-*sn*-glycero-3-phosphocholine (DOPC) and 1,2-dioleoyl-*sn*-glycero-3-phosphoethanolamine-N-(biotinyl) (DOPE-Biotin) (Avanti Polar Lipids) were prepared as follows. 0.5 ml of DOPC (25 mg/ml chloroform) was mixed with 5 μl of DOPE-biotin (25 mg/ml chloroform) in a glass test tube and most of the solvent removed via evaporation under a nitrogen flow. The remaining solvent was removed by drying

in a SpeedVac (Savant) at 42°C for 1 hr followed by a further 1 hr at room temperature. 2.5 ml of degassed TK150 buffer (25 mM Tris-HCl pH 7.5, 150 mM KCl) was then added, and the lipids stored and covered under nitrogen gas overnight. The lipids were then resuspended by vortexing and sonicated (70–80 watts, 30 s on, 10 s off) in a cup horn with water chiller set to 16°C (QSonica) until transparent. The resulting solution of SUVs was then filtered through a 0.22 μm filter, aliquoted, and stored under nitrogen gas at 4°C for up to 4 weeks.

To prepare biotinylated salmon sperm DNA for DNA-carpets 10 mg/ml salmon sperm DNA (Thermo Fisher) was sonicated for 5 min (110 watts, 10 s on, 10 s off) to produce short fragments. Sonicated salmon sperm DNA was then diluted to 1 mg/ml in Terminal Transferase buffer (NEB) with 0.25 mM CoCl_2 , 40 μM Biotin-14-dCTP (Thermo Fisher), and 1 unit/ μl Terminal Transferase (NEB). The DNA was incubated at 37°C for 30 min, and then the reaction stopped by heat inactivation at 75°C for 20 min. Free Biotin-14-dCTP was removed by extensive buffer exchange with TE buffer (10 mM Tris-HCl pH 8, 0.1 mM EDTA) in a 100 kDa Amicon Ultra spin concentrator (Millipore). The biotinylated DNA was then concentrated to ~10 mg/ml and stored at –20°C until needed.

To assemble a DNA-carpet, the DOPC-DOPE-biotin SUV solution was diluted to 1 mg/ml in 500 μl degassed TN150MC buffer (25 mM Tris-HCl pH7.5, 150 mM NaCl, 5 mM MgCl_2 , 0.1 mM CaCl_2) and warmed to 37°C. Approximately 300 μl of SUV solution was then infused into a pre-warmed flow cell and incubated at 37°C for 1 hr. Excess SUVs were washed out with 500 μl warmed, degassed TN150MC buffer at 100 $\mu\text{l}/\text{min}$. 300 μl of a solution of 1 mg/ml neutravidin (Thermo Fisher) in warmed, degassed TN150MC buffer was then infused at a rate of 100 $\mu\text{l}/\text{min}$ into the flow cell and incubated at 37°C for 30 min. Excess neutravidin was washed out with TN150MC buffer as above, and the flow cell infused with 100 μl of a solution containing 1 mg/ml biotinylated sonicated salmon sperm DNA (as prepared above) in warmed, degassed TN150MC buffer, and incubated at 37°C for 30 min. The ports of the flow cell were sealed with parafilm and stored at 4°C for up to a week.

Prior to use, excess DNA was removed by infusion of 300 μl 0.22 μm filtered and degassed TIRFM buffer (50 mM HEPES-KOH pH 7.5, 300 mM K-glutamate, 50 mM NaCl, 10 mM MgCl_2 , 0.1 mM CaCl_2 , 2 mM DTT, 0.1 mg/ml α -casein, 0.6 mg/ml ascorbic acid, 10% glycerol) with addition of 1 mg/ml α -casein and 1 mM ATP γ S and the flow cell incubated at room temperature for 30 min.

Conversion of the fluorescence signal detected in TIRF microscopy to the DNA-carpet-bound protein densities was done following the procedure described in the legend of Figure 2—figure supplement 4 in [Vecchiarelli et al., 2016](#).

Fluorescence recovery after photobleaching (FRAP)

For FRAP experiments, 488 nm solid-state and 630 nm diode lasers were focused to the back focal plane of the objective through an appropriate dichroic mirror (Di01-R405/488/561/635-25x36, Semrock) through the objective lens to illuminate a ~5 or ~10 μm (for 488 nm or 630 nm, respectively) diameter spot in the center of the sample area. The laser power was adjusted for ~80% bleaching with 5 s exposure for the eGFP or Alexa 647 signals, and four cycles of bleaching/recovery were recorded for each sample and averaged.

Magnetic tweezers-based DNA condensation assay

The magnetic tweezers setup and assays conducted with it were performed as previously described ([Seol and Neuman, 2011](#); [Seol et al., 2016](#)).

The ability of ParB_F to condense *parS_F*-containing DNA (spDNA) was tested by a custom-built magnetic tweezers setup. In brief, two permanent magnets were used to apply force to micron-sized magnetic beads individually tethered to the coverslip of a one inlet flow cell by 5 kb pET28a plasmid-derived DNA tethers. The distance the magnets were held from the beads, and hence the force exerted upon them was controlled by a linear motor that vertically positions the magnets.

Five kilo-base DNA substrates were generated by PCR using either pET28a-*parS_F* plasmid (for *parS_F*-containing DNA) or pET28a as templates. pET28-*parS_F* DNA plasmid was generated by cloning 570 bp DNA segment containing 12 repeats of *parS_F* native sequence from F-plasmid into pET28a between the BamHI and SphI restriction sites.

Primers used for the PCR contained an extra non-complementary 15 nt at their 5' ends to encode BsaI restriction sites. The PCR yields a 5.2 kb product incorporating two BsaI restriction sites at its termini. Digestion of this product was followed by ligation with 500 bp DNA 'handles' containing

either multiple biotin or digitoxin labels. These handles were also generated by Taq-based PCR using pBlueScript II KS as the template, pBlueScript II KS forward (5'- GCT GGG TCT CGG TTG TTC CCT TTA GTG AGG GTT AAT TG) and pBlueScript II KS reverse (5'- GCT GGG TCT CGT GGT TTC CCT TTA GTG AGG GTT AAT TG) primers and either 60 μ M biotin-16-dUTP or digoxigenin-11-dUTP (Roche). This results in a 5 kb DNA tether, which can be attached to a streptavidin-coated magnetic bead at one end and an anti-digoxigenin coverslip surface at the other.

ParB_F samples were prepared in modified ATPase buffer (50 mM HEPES.KOH pH 7.5, 100 mM KCl, 5 mM MgCl₂, 2 mM DTT, 10 mg/ml BSA, and 0.1% Tween-20) and infused into a flow cell containing tethered magnetic beads held at 5 pN of force. After the chamber was filled, the flow was stopped, and the force reduced to 0.05 pN. The height of beads was tracked by analysis of diffraction rings generated by illumination of the beads from above and observed with an objective positioned below the flow cell. The extent of condensation by ParB was monitored by the decrease in the height of the beads at 0.05 and 5 pN as compared to controls without protein.

Acknowledgements

We are grateful to helpful suggestions and discussion of our colleagues Barbara Funnell, David Lane, Michiyo Mizuuchi, Andrea Volante, Min Li, Masaki Osawa, William Carlquist, and Shannon Mckie, to Esme Neuman for help in preparation of **Figures 1** and **7**, and to Min Li for help in preparation of **Figure 2—figure supplement 3**. We thank Stephan Gruber and his colleagues for sharing their findings with us prior to publication. This work was supported by the intramural research fund for National Institute of Diabetes and Digestive and Kidney Diseases (KM), and the National Heart, Lung, and Blood Institute (KCN), National Institutes of Health, Department of Human Services.

Additional information

Funding

Funder	Grant reference number	Author
NIDDK	Intramural Research Fund	Kiyoshi Mizuuchi
NHLBI	Intramural Research Fund	Keir C Neuman

The funders had no role in study design, data collection and interpretation, or the decision to submit the work for publication.

Author contributions

James A Taylor, Conceptualization, Data curation, Formal analysis, Writing - original draft, Writing - review and editing; Yeonee Seol, Data curation, Formal analysis, Writing - original draft, Writing - review and editing; Jagat Budhathoki, Data curation, Formal analysis; Keir C Neuman, Kiyoshi Mizuuchi, Conceptualization, Resources, Formal analysis, Supervision, Funding acquisition, Writing - review and editing

Author ORCIDs

Keir C Neuman  <http://orcid.org/0000-0002-0863-5671>

Kiyoshi Mizuuchi  <https://orcid.org/0000-0001-8193-9244>

Decision letter and Author response

Decision letter <https://doi.org/10.7554/eLife.65651.sa1>

Author response <https://doi.org/10.7554/eLife.65651.sa2>

Additional files

Supplementary files

- Source data 1. Excel file containing all source data. One Excel file with 19 sheets: Numerical data for **Figure 2A-E**, **Figure 2F,G**, **Figure 2—figure supplement 2**, **Figure 2—figure supplement 4**,

Figure 3A-C, Figure 3D, Figure 4A-D, Figure 4E, Figure 4—figure supplement 1B, Figure 4—figure supplement 2A-D, Figure 5A-D, Figure 5E,F, Figure 5—figure supplement 1B, Figure 5—figure supplement 2, Figure 6A, Figure 6B - left, Figure 6B - right, Figure 6C, Figure 6—figure supplement 1A, Figure 6—figure supplement 1B, Figure 6—figure supplement 2, Figure 6—figure supplement 3.

- Transparent reporting form

Data availability

All data generated or analysed during this study are included in the manuscript and supporting files. Source data files have been provided for all relevant figures.

References

- Ah-Seng Y, Lopez F, Pasta F, Lane D, Bouet JY. 2009. Dual role of DNA in regulating ATP hydrolysis by the SopA partition protein. *Journal of Biological Chemistry* **284**:30067–30075. DOI: <https://doi.org/10.1074/jbc.M109.044800>, PMID: 19740757
- Ah-Seng Y, Rech J, Lane D, Bouet JY. 2013. Defining the role of ATP hydrolysis in Mitotic segregation of bacterial plasmids. *PLOS Genetics* **9**:e1003956. DOI: <https://doi.org/10.1371/journal.pgen.1003956>, PMID: 24367270
- Baxter JC, Funnell BE. 2014. Plasmid partition mechanisms. *Microbiology Spectrum* **2**:1. DOI: <https://doi.org/10.1128/microbiolspec.PLAS-0023-2014>
- Bouet JY, Surtees JA, Funnell BE. 2000. Stoichiometry of P1 plasmid partition complexes. *Journal of Biological Chemistry* **275**:8213–8219. DOI: <https://doi.org/10.1074/jbc.275.11.8213>, PMID: 10713146
- Breier AM, Grossman AD. 2007. Whole-genome analysis of the chromosome partitioning and sporulation protein SpoJ (ParB) reveals spreading and origin-distal sites on the *Bacillus subtilis* chromosome. *Molecular Microbiology* **64**:703–718. DOI: <https://doi.org/10.1111/j.1365-2958.2007.05690.x>, PMID: 17462018
- Chen BW, Lin MH, Chu CH, Hsu CE, Sun YJ. 2015. Insights into ParB spreading from the complex structure of SpoJ and parS. *PNAS* **112**:6613–6618. DOI: <https://doi.org/10.1073/pnas.1421927112>, PMID: 25964325
- Davey MJ, Funnell BE. 1994. The P1 plasmid partition protein ParA. A role for ATP in site-specific DNA binding. *Journal of Biological Chemistry* **269**:29908–29913. DOI: [https://doi.org/10.1016/S0021-9258\(18\)43967-1](https://doi.org/10.1016/S0021-9258(18)43967-1), PMID: 7961987
- Davis MA, Martin KA, Austin SJ. 1992. Biochemical activities of the parA partition protein of the P1 plasmid. *Molecular Microbiology* **6**:1141–1147. DOI: <https://doi.org/10.1111/j.1365-2958.1992.tb01552.x>, PMID: 1534133
- Ebersbach G, Gerdes K. 2004. Bacterial mitosis: partitioning protein ParA oscillates in spiral-shaped structures and positions plasmids at mid-cell. *Molecular Microbiology* **52**:385–398. DOI: <https://doi.org/10.1111/j.1365-2958.2004.04002.x>, PMID: 15066028
- Fung E, Bouet JY, Funnell BE. 2001. Probing the ATP-binding site of P1 ParA: partition and repression have different requirements for ATP binding and hydrolysis. *The EMBO Journal* **20**:4901–4911. DOI: <https://doi.org/10.1093/emboj/20.17.4901>, PMID: 11532954
- Graham TG, Wang X, Song D, Etson CM, van Oijen AM, Rudner DZ, Loparo JJ. 2014. ParB spreading requires DNA bridging. *Genes & Development* **28**:1228–1238. DOI: <https://doi.org/10.1101/gad.242206.114>, PMID: 24829297
- Hatano T, Yamaichi Y, Niki H. 2007. Oscillating focus of SopA associated with filamentous structure guides partitioning of F plasmid. *Molecular Microbiology* **64**:1198–1213. DOI: <https://doi.org/10.1111/j.1365-2958.2007.05728.x>, PMID: 17542915
- Helsberg M, Eichenlaub R. 1986. Twelve 43-base-pair repeats map in a cis-acting region essential for partition of plasmid mini-F. *Journal of Bacteriology* **165**:1043–1045. DOI: <https://doi.org/10.1128/jb.165.3.1043-1045.1986>, PMID: 3949712
- Hu L, Vecchiarelli AG, Mizuuchi K, Neuman KC, Liu J. 2017. Brownian ratchet mechanism for faithful segregation of Low-Copy-Number plasmids. *Biophysical Journal* **112**:1489–1502. DOI: <https://doi.org/10.1016/j.bpj.2017.02.039>, PMID: 28402891
- Ivanov V, Mizuuchi K. 2010. Multiple modes of interconverting dynamic pattern formation by bacterial cell division proteins. *PNAS* **107**:8071–8078. DOI: <https://doi.org/10.1073/pnas.0911036107>, PMID: 20212106
- Jalal AS, Tran NT, Le TB. 2020. ParB spreading on DNA requires cytidine triphosphate in vitro. *eLife* **9**:e53515. DOI: <https://doi.org/10.7554/eLife.53515>, PMID: 32077854
- Le Gall A, Cattoni DI, Guilhas B, Mathieu-Demazière C, Oudjedi L, Fiche J-B, Rech J, Abrahamsson S, Murray H, Bouet J-Y, Nollmann M. 2016. Bacterial partition complexes segregate within the volume of the nucleoid. *Nature Communications* **7**:12107. DOI: <https://doi.org/10.1038/ncomms12107>
- Leonard TA, Butler PJ, Löwe J. 2005. Bacterial chromosome segregation: structure and DNA binding of the soj dimer—a conserved biological switch. *The EMBO Journal* **24**:270–282. DOI: <https://doi.org/10.1038/sj.emboj.7600530>, PMID: 15635448

- Lim HC, Surovtsev IV, Beltran BG, Huang F, Bewersdorf J, Jacobs-Wagner C. 2014. Evidence for a DNA-relay mechanism in ParABS-mediated chromosome segregation. *eLife* **3**:e02758. DOI: <https://doi.org/10.7554/eLife.02758>, PMID: 24859756
- Lutkenhaus J. 2012. The ParA/MinD family puts things in their place. *Trends in Microbiology* **20**:411–418. DOI: <https://doi.org/10.1016/j.tim.2012.05.002>, PMID: 22672910
- McLeod BN, Allison-Gamble GE, Barge MT, Tonthat NK, Schumacher MA, Hayes F, Barillà D. 2017. A three-dimensional ParF meshwork assembles through the nucleoid to mediate plasmid segregation. *Nucleic Acids Research* **45**:3158–3171. DOI: <https://doi.org/10.1093/nar/gkw1302>, PMID: 28034957
- Modrich P, Zabel D. 1976. EcoRI endonuclease. Physical and catalytic properties of the homogenous enzyme. *Journal of Biological Chemistry* **251**:5866–5874. DOI: [https://doi.org/10.1016/S0021-9258\(17\)33032-6](https://doi.org/10.1016/S0021-9258(17)33032-6)
- Mori H, Mori Y, Ichinose C, Niki H, Ogura T, Kato A, Hiraga S. 1989. Purification and characterization of SopA and SopB proteins essential for F plasmid partitioning. *Journal of Biological Chemistry* **264**:15535–15541. DOI: [https://doi.org/10.1016/S0021-9258\(19\)84863-9](https://doi.org/10.1016/S0021-9258(19)84863-9), PMID: 2670941
- Motallebi-Veshareh M, Rouch DA, Thomas CM. 1990. A family of ATPases involved in active partitioning of diverse bacterial plasmids. *Molecular Microbiology* **4**:1455–1463. DOI: <https://doi.org/10.1111/j.1365-2958.1990.tb02056.x>, PMID: 2149583
- Murray H, Ferreira H, Errington J. 2006. The bacterial chromosome segregation protein Spo0J spreads along DNA from parS nucleation sites. *Molecular Microbiology* **61**:1352–1361. DOI: <https://doi.org/10.1111/j.1365-2958.2006.05316.x>, PMID: 16925562
- Osorio-Valeriano M, Altegoer F, Steinchen W, Urban S, Liu Y, Bange G, Thanbichler M. 2019. ParB-type DNA segregation proteins are CTP-Dependent molecular switches. *Cell* **179**:1512–1524. DOI: <https://doi.org/10.1016/j.cell.2019.11.015>, PMID: 31835030
- Pillet F, Sanchez A, Lane D, Anton Leberre V, Bouet JY. 2011. Centromere binding specificity in assembly of the F plasmid partition complex. *Nucleic Acids Research* **39**:7477–7486. DOI: <https://doi.org/10.1093/nar/gkr457>, PMID: 21653553
- Ravin NV, Kuprianov VV, Gilcrease EB, Casjens SR. 2003. Bidirectional replication from an internal ori site of the linear N15 plasmid prophage. *Nucleic Acids Research* **31**:6552–6560. DOI: <https://doi.org/10.1093/nar/gkg856>, PMID: 14602914
- Ringgaard S, van Zon J, Howard M, Gerdes K. 2009. Movement and equi-positioning of plasmids by ParA filament disassembly. *PNAS* **106**:19369–19374. DOI: <https://doi.org/10.1073/pnas.0908347106>, PMID: 19906997
- Rodionov O, Lobočka M, Yarmolinsky M. 1999. Silencing of genes flanking the P1 plasmid centromere. *Science* **283**:546–549. DOI: <https://doi.org/10.1126/science.283.5401.546>, PMID: 9915704
- Sanchez A, Cattoni DI, Walter JC, Rech J, Parmeggiani A, Nollmann M, Bouet JY. 2015. Stochastic Self-Assembly of ParB proteins builds the bacterial DNA segregation apparatus. *Cell Systems* **1**:163–173. DOI: <https://doi.org/10.1016/j.cels.2015.07.013>, PMID: 27135801
- Scholefield G, Whiting R, Errington J, Murray H. 2011. Spo0J regulates the oligomeric state of soj to trigger its switch from an activator to an inhibitor of DNA replication initiation. *Molecular Microbiology* **79**:1089–1100. DOI: <https://doi.org/10.1111/j.1365-2958.2010.07507.x>, PMID: 21235642
- Schumacher MA, Piro KM, Xu W. 2010. Insight into F plasmid DNA segregation revealed by structures of SopB and SopB-DNA complexes. *Nucleic Acids Research* **38**:4514–4526. DOI: <https://doi.org/10.1093/nar/gkq161>, PMID: 20236989
- Schumacher MA, Funnell BE. 2005. Structures of ParB bound to DNA reveal mechanism of partition complex formation. *Nature* **438**:516–519. DOI: <https://doi.org/10.1038/nature04149>, PMID: 16306995
- Seol Y, Strub MP, Neuman KC. 2016. Single molecule measurements of DNA helicase activity with magnetic tweezers and t-test based step-finding analysis. *Methods* **105**:119–127. DOI: <https://doi.org/10.1016/j.ymeth.2016.04.030>, PMID: 27131595
- Seol Y, Neuman KC. 2011. Magnetic tweezers for single-molecule manipulation. *Methods in Molecular Biology* **783**:265–293. DOI: https://doi.org/10.1007/978-1-61779-282-3_15, PMID: 21909894
- Soh YM, Davidson IF, Zamuner S, Basquin J, Bock FP, Taschner M, Veening JW, De Los Rios P, Peters JM, Gruber S. 2019. Self-organization of parS centromeres by the ParB CTP hydrolase. *Science* **366**:1129–1133. DOI: <https://doi.org/10.1126/science.aay3965>, PMID: 31649139
- Song D, Rodrigues K, Graham TGW, Loparo JJ. 2017. A network of Cis and trans interactions is required for ParB spreading. *Nucleic Acids Research* **45**:7106–7117. DOI: <https://doi.org/10.1093/nar/gkx271>, PMID: 28407103
- Sugawara T, Kaneko K. 2011. Chemophoresis as a driving force for intracellular organization: theory and application to plasmid partitioning. *Biophysics* **7**:77–88. DOI: <https://doi.org/10.2142/biophysics.7.77>
- Taylor JA, Pastrana CL, Butterer A, Pernstich C, Gwynn EJ, Sobott F, Moreno-Herrero F, Dillingham MS. 2015. Specific and non-specific interactions of ParB with DNA: implications for chromosome segregation. *Nucleic Acids Research* **43**:719–731. DOI: <https://doi.org/10.1093/nar/gku1295>, PMID: 25572315
- Vecchiarelli AG, Han YW, Tan X, Mizuuchi M, Ghirlando R, Biertümpfel C, Funnell BE, Mizuuchi K. 2010. ATP control of dynamic P1 ParA-DNA interactions: a key role for the nucleoid in plasmid partition. *Molecular Microbiology* **78**:no–91. DOI: <https://doi.org/10.1111/j.1365-2958.2010.07314.x>, PMID: 20659294
- Vecchiarelli AG, Mizuuchi K, Funnell BE. 2012. Surfing biological surfaces: exploiting the nucleoid for partition and transport in Bacteria. *Molecular Microbiology* **86**:513–523. DOI: <https://doi.org/10.1111/mmi.12017>, PMID: 22934804

- Vecchiarelli AG**, Hwang LC, Mizuuchi K. 2013. Cell-free study of F plasmid partition provides evidence for cargo transport by a diffusion-ratchet mechanism. *PNAS* **110**:E1390–E1397. DOI: <https://doi.org/10.1073/pnas.1302745110>, PMID: 23479605
- Vecchiarelli AG**, Neuman KC, Mizuuchi K. 2014. A propagating ATPase gradient drives transport of surface-confined cellular cargo. *PNAS* **111**:4880–4885. DOI: <https://doi.org/10.1073/pnas.1401025111>, PMID: 24567408
- Vecchiarelli AG**, Li M, Mizuuchi M, Hwang LC, Seol Y, Neuman KC, Mizuuchi K. 2016. Membrane-bound MinDE complex acts as a toggle switch that drives min oscillation coupled to cytoplasmic depletion of MinD. *PNAS* **113**:E1479–E1488. DOI: <https://doi.org/10.1073/pnas.1600644113>, PMID: 26884160
- Watanabe E**, Wachi M, Yamasaki M, Nagai K. 1992. ATPase activity of SopA, a protein essential for active partitioning of F plasmid. *Molecular and General Genetics MGG* **234**:346–352. DOI: <https://doi.org/10.1007/BF00538693>, PMID: 1406581
- Yamaichi Y**, Niki H. 2000. Active segregation by the *Bacillus subtilis* partitioning system in *Escherichia coli*. *PNAS* **97**:14656–14661. DOI: <https://doi.org/10.1073/pnas.97.26.14656>, PMID: 11121066